

Hidden Connectivity Structures Control Collective Network Dynamics

Lorenzo Tiberi^{1,2,3}, David Dahmen¹, and Moritz Helias^{1,2,3}

¹*Institute of Neuroscience and Medicine (INM-6) and Institute for Advanced Simulation (IAS-6) and JARA-Institute Brain Structure-Function Relationships (INM-10), Jülich Research Centre, Jülich, Germany*

²*Institute for Theoretical Solid State Physics, RWTH Aachen University, 52074 Aachen, Germany and*

³*Center for Advanced Simulation and Analytics, Forschungszentrum Jülich, 52425 Jülich, Germany*

Many observables of brain dynamics appear to be optimized for computation. Which connectivity structures underlie this fine-tuning? We propose that many of these structures are naturally encoded in the space that more directly relates to network dynamics – the space of the connectivity eigenmodes. We develop a mathematical theory to impose eigenmode structures on connectivity, systematically characterizing their effect on network dynamics. We find the density of nearly-critical eigenvalues to be a particularly fundamental structure. It flexibly controls the power-law scaling of dynamical observables, in analogy with the system’s spatial dimension in classical critical phenomena. This mechanism provides control over observables which are found to be fine-tuned in brain networks, but remained so far unexplained by traditionally studied structures, such as connectivity motifs. Specifically, the slope of the principal component spectrum of neural activity can be fine-tuned, as observed in primary visual cortex of mice. Furthermore, a novel transition between high and low dimensional activity allows for a wide and flexible tuning of dimensionality, as observed throughout cortex. The here discovered structures thus largely complement motifs. In fact, they are of a different, collective nature: they are not reflected by any local motif configuration. This result shows that many functionally relevant structures can remain hidden within the apparent randomness of highly heterogeneous cortical circuits. Our methods enable revealing these structures and investigate their effect on network dynamics.

I. INTRODUCTION

Network dynamics is a central topic of contemporary physics, due to its ability to describe a wide variety of biological, social and artificial systems [1]. Indeed, through different arrangements of their connectivity, networks are able to manifest the most disparate complex behaviors. A prime example are neural networks: local circuits across different cortical areas specialize their connectivity to implement very diverse computational functions [2], such as motor control, object recognition or abstract reasoning.

Many observables of brain dynamics indeed appear to be fine-tuned for specific computational needs. For example, in the primary visual cortex (V1) of mice, the principal component (PC) spectrum of neuronal activity is found to have an optimal slope for image encoding [3]. At the same time, dynamical observables are tuned differently and flexibly across cortical areas, depending on the area’s computational needs. For example, neuronal activity is found to be either low [4–6] or high dimensional [3, 7] in different regions of cortex [8], with both high and low dimensionality optimizing different computational functions.

A fundamental quest of neuroscience is to identify the connectivity structures that allow for such flexible, yet precise tuning of network dynamics. This is complicated by the fact that connectivity in cortical microcircuits is highly heterogeneous, appearing to a large extent as random, and thus strikingly similar across cortical areas [9]. Therefore, the challenge is often to find structure *within* randomness, that is structure in the connectivity statistics. In order to provide focus and direction to this complex search, an important role of theory is to answer this

first-principles question: What are the minimal and fundamental structures in a connectivity statistics, which allow networks to fine-tune their dynamics?

One of such structures has been recently identified in motifs [10–12]: minimal connectivity patterns between few neurons, which occur with higher chance than random [13]. Second order motifs have been shown to have some control over neuronal activity, such as its dimensionality [10–12]. Still, there remain many of the aforementioned network behaviors which do not seem to be explainable by these structures alone. For example, it was shown that second order motifs cannot fine-tune the power-law decay of the PC spectrum of neuronal activity [11]. Also, near criticality, where this and other power-laws ubiquitously observed in brain dynamics emerge [3, 14–16], neuronal activity is always low-dimensional, and cannot be tuned to be high dimensional [12]. This naturally raises a question: Are there other fundamental connectivity structures that we are missing, which can account for these unexplained behaviors?

Here we identify such structures by proposing a paradigm shift: If motifs are *local* structures, encoded in the connections between few neurons, we argue that there is also a fundamentally different type of structures, which are intrinsically *collective*. These are encoded in the space that naturally relates to collective network dynamics - the space of the connectivity eigenmodes. Various works have highlighted the importance of eigenmode structures. For example, specific forms of eigenvalue distributions are shown to emerge after training [17], and the angle between eigenvectors often has important functional consequences, such as in low-rank connectivity structures [18]. However, thus far the field

is lacking a mathematical framework to directly impose eigenmode structures on heterogeneous connectivity matrices, allowing to systematically characterize their effect on network dynamics.

We thus develop a novel theory for large random connectivity matrices with specifiable eigenmode statistics. In particular, as outlined in Section II, we can specify the degree of non-orthogonality between eigenvectors, and the shape of the eigenvalue distribution. This allows us to rigorously characterize network dynamics as a function of these eigenmode structures. As shown in Section III, we find the shape of the eigenvalue distribution to be a particularly effective structure, controlling dynamical observables such as the autocorrelation, autoresponse, PC spectrum, and dimensionality of neuronal activity. Specifically, the scaling exponents of these quantities are directly controlled by the scaling exponent of the density of nearly critical eigenvalues, in analogy to how the system's spatial dimension affects scaling in classical critical phenomena (III A). In particular, this mechanism can account for the widely observed fine-tuning of functionally relevant measures of network dynamics, which so far remained unexplained by motif structures alone: varying the density of nearly critical eigenvalues, the PC spectrum can be fine-tuned into its optimal slope for stimulus encoding (III C), as observed in V1 of mice [3], and dimensionality of neural activity can flexibly transition between both the high and the low dimensional regimes observed throughout cortex [3–8], while remaining at the critical point (III C).

From the space of eigenmodes, we also derive the connectivity statistics in the more direct space of synaptic strengths. The result, presented in Section IV, shows how the here considered eigenmode structures are of a fundamentally different nature than motifs, complementing them not only from a functional, but also from a structural perspective. Indeed, these structures are intrinsically collective: to leading order in the number of neurons, they are not reflected by local motif configurations, and the connectivity always appears as random Gaussian (see Fig. 1). The result provides an intriguing insight into the apparent paradox of structure within randomness: there can in fact be much structure hidden in the eigenmodes of an apparently random Gaussian connectivity, which has profound effects on the network dynamics. This structure remains hidden to a local motifs analysis. However, it can be revealed by a more collective analysis of the connectivity eigenmodes.

II. SETTING

We consider the recurrent network of linear rate neurons

$$\tau \partial_t x_i(t) = -x_i(t) + \sum_j J_{ij} x_j(t) + \xi_i(t), \quad (1)$$

where $x_i(t)$ is the rate activity of neuron i at time t ; $i = 1, \dots, N$. Here J_{ij} describes the connection from neuron j to i and τ is the characteristic timescale of neuronal response. The network is driven by Gaussian white noise $\xi_i(t)$, with zero mean and variance $\langle \xi_i(t) \xi_j(t') \rangle = D \delta_{ij} \delta(t - t')$. In the following, we consider Eq. (1) in dimensionless units, setting $\tau = D = 1$. In the linear regime, the second order statistics of various network models, comprising integrate-fire and inhomogeneous Poisson neurons, is well captured by Eq. (1) [19–23]. For this reason, Eq. (1) is a minimal model for characterizing network dynamics analytically, as a function of J [11, 12, 22, 24].

Local cortical circuits present strong variability in their connectivity. A common approach is to model such variability as disorder, choosing J as a random matrix. Most likely, brain networks are not completely disordered: we expect them to have some function, thus some underlying connectivity structure. In the random connectivity setting, information about the network function or structure can be included in the model through the choice of statistics for J .

To constrain the connectivity statistics, previous works have focused on the observed abundance of local connectivity patterns involving few neurons, such as the connectivity motifs [13] depicted in Fig. 1. In particular, analytical studies characterizing the effect of motifs on network dynamics are typically constrained to second order motifs [10–12]. The relative abundance of a motif with respect to a completely random network can be modeled by a non-vanishing moment of the elements of J involved in the motif [11]. In an archetypal approach [25, 26], for example, J is assumed Gaussian with statistics

$$g^2 \equiv N \langle J_{ij}^2 \rangle \quad \tau \equiv \langle J_{ij} J_{ji} \rangle / \langle J_{ij}^2 \rangle, \quad i \neq j. \quad (2)$$

Two parameters are present: the synaptic gain g models the overall strength of recurrent connections, while the degree of (anti)symmetry τ controls correlations between reciprocal connections, which can be associated with an abundance of reciprocal motifs. Throughout the manuscript, we will refer to this connectivity choice as the archetypal choice for J and use it for comparison with our approach. Note that any other second order motif (those shown in the top row of 1 with a bar on top) can always be introduced later as a low rank perturbation to this bulk connectivity, and their effect on network dynamics can be characterized by a finite number of outliers perturbing the bulk spectrum of the neuronal activity's covariance matrix [11]. Therefore, here we focus on the bulk connectivity.

As discussed in Section I, local motifs can only partially account for the optimal fine-tuning of dynamics observed in cortical networks. To fill this gap, here we introduce the study of another fundamental type of collective, rather than local structures. These are encoded in the space that naturally controls network dynamics – the space of eigenmodes. The connectivity J can always

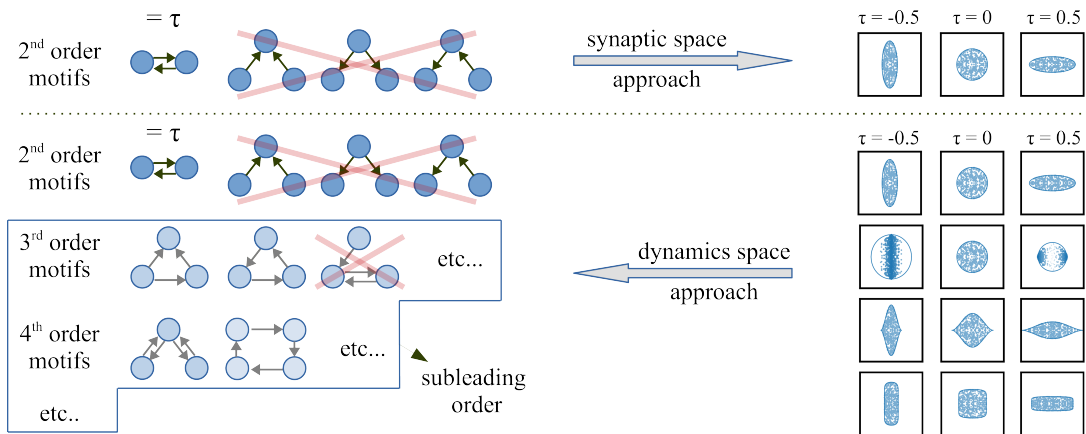


Figure 1. Schematic representation of the traditional synaptic space approach vs our dynamics space approach. Top: synaptic space approach. Some motif statistics are assumed (left) and the eigenmode statistics (right) are derived. Specifically, here we show an archetypal approach which assumes only the presence of second order reciprocal motifs (here parameterized by τ , Eq. (2)). The corresponding eigenvalue distribution is uniform on an ellipse. The eigenvalues are relatively more spread along the real or the imaginary axis depending on the value of τ . Bottom: dynamics space approach. We specify the eigenmode statistics, in particular allowing for any desired shape of the eigenvalue distribution (right). The derived synaptic statistics (left) to leading order only predict reciprocal motifs, as in the archetypal approach. These are parameterized again by the relative spread τ of the eigenvalues, here generalized to any distribution shape. Higher order motif structures are present, but are subleading in the number of neurons. Thus, the synaptic structures responsible for different shapes of the eigenvalue distribution (thus different dynamics) are hidden to a motifs analysis.

be decomposed into its eigenvalues λ_α and right eigenvectors V_α as

$$J_{ij} = \sum_{\alpha=1}^N V_{i\alpha} \lambda_\alpha V_{\alpha j}^{-1}, \quad (3)$$

were the left eigenvectors' matrix V^{-1} is the inverse of the right eigenvectors' matrix V . For typical random connectivity matrices, this decomposition can be performed without loss of generality (see Appendix A1). Eigenvalues and eigenvectors have a direct dynamical interpretation: a linear combination of neurons $\sum_i V_{\alpha i}^{-1} x_i$ represents a collective mode of the linearized neuronal activity, with dynamical response $\propto \exp(-(1 - \lambda_\alpha)t)$. Thus, calling an eigenvalue $\lambda = \lambda_x + i\lambda_y$, the associated mode has decay constant $1 - \lambda_x$ and oscillation frequency λ_y . The distribution of eigenvalues therefore characterizes the dynamical repertoire available to the network, while the overlap between eigenvectors characterizes how much the network input co-excites different eigenmodes [27]. Both the shape of the eigenvalue distribution and the eigenvectors' overlap are therefore important structural properties of connectivity, which are indeed shown to be associated with network function [17, 18].

Through the archetypal choice of J , these eigenmode structures are implicitly fixed: eigenvalues are uniformly distributed on an ellipse centered in the complex plane [26] (Fig. 1, top), while eigenvectors are strongly non-orthogonal, as discussed later in greater detail. Given their high relevance for network dynamics, however, here we want to explicitly constrain the form of these connec-

tivity structures to systematically characterize their impact on neural activity. Concretely, we approach connectivity modeling in a direction symmetric to the archetypal approach (Fig. 1): In the archetypal *synaptic space approach*, one specifies the statistics of synaptic strengths (the entries of J) and later derives the corresponding eigenmode statistics; in our *dynamics space approach*, we first specify the eigenmode statistics and later derive the synaptic strength statistics. We define the eigenmode statistics as

$$\lambda \sim p(\lambda) \quad (4)$$

$$V = O + \nu G \quad (5)$$

Eq. (4) states that λ can be drawn from a distribution p of any arbitrary shape, provided its moments are bounded. In particular, one is not constrained to a uniform elliptical distribution as in the archetypal approach (see Fig. 1). In turn, we will show in Section III how the shape of p is directly linked to the dynamics, in particular to power-law exponents ubiquitously observed in cortical networks, and thus can be fixed according to a certain observed or desired network behavior. The eigenvalues are drawn independently, following the same simplicity principle typically applied in the synaptic space approach: introducing minimal information in an otherwise disordered connectivity.

Following the same principle, we want to be agnostic with regard to the direction that a certain eigenmode takes in neuronal space. The eigenvector matrix V is therefore drawn independently from the eigenvalues. Eq. (5) defines it as a combination of a unitary and

a complex Gaussian random matrix O and G , respectively, with interpolation parameter $\nu \in [0, 1)$ controlling the degree of non-normality of the network. A precise definition of O and G can be found in A 1. Intuitively, varying ν from 0 to 1 controls whether eigenmodes are orthogonal to each other ($\nu = 0$), or can take on more and more random, overlapping directions ($\nu \rightarrow 1$). The value $\nu = 1$ is an upper limit at which eigenvectors are too overlapping and the synaptic gain g diverges (see Section IV and Appendix A 2).

A difference with the archetypal case of Gaussian J is that, there, eigenvalues and eigenvectors are found to be tightly correlated, and eigenvectors are in a strongly non-orthogonal regime, similar to choosing $\nu \sim 1$ in our ensemble. In Section IV we show that, in this strongly non-normal regime, a fine-tuned correlation structure is necessary to contrast the strong eigenvectors' overlap and thus keep the synaptic gain g of $\mathcal{O}(1)$. We then devise a method to initialize connectivities with such fine-tuned correlation structure, while still allowing for any shape of the eigenvalue distribution. In this way, through numerical simulations, we are able to characterize also the strongly non-normal regime. Including this strongly non-normal ensemble, our study therefore encompasses the archetypal case of Gaussian J .

As we show in Section III, varying the shape of the eigenvalue distribution causes a wide range of different dynamical behaviors. Surprisingly, however, we find this is not reflected by the leading order statistics of synaptic strengths. Just as for the archetypal connectivity, we find the synaptic strength statistics to be Gaussian, with only reciprocal motifs. In terms of the eigenmode statistics, the leading order synaptic strength statistics are given by

$$g^2 = \frac{1 + \nu^2}{1 - \nu^2} \left(\langle \lambda_x^2 \rangle_\lambda + \langle \lambda_y^2 \rangle_\lambda \right) \quad (6)$$

$$\tau = \frac{1 - \nu^2}{1 + \nu^2} \frac{\langle \lambda_x^2 \rangle_\lambda - \langle \lambda_y^2 \rangle_\lambda}{\langle \lambda_x^2 \rangle_\lambda + \langle \lambda_y^2 \rangle_\lambda} \quad (7)$$

where $\langle \cdot \rangle_\lambda$ denotes statistical averaging over the random variable λ . Other second order motifs are absent. Higher order motifs are present, but only with a probability that is vanishingly small in the number of neurons, and are therefore very hard to detect. As a result, connectivities with the same leading order motif structure can correspond to different eigenmode structures, thus to very different network dynamics, as exemplified in Fig. 2. In other words, there are structures that have a strong impact in shaping the network dynamics, while remaining hidden in the synaptic strength statistics of an apparently random Gaussian connectivity. More precisely, these structures remain hidden to a motif analysis, as they cannot be reduced to the generic abundance of local connectivity patterns. However, they become apparent to a more collective analysis of the connectivity's spectral properties, in particular of its eigenvalue distri-

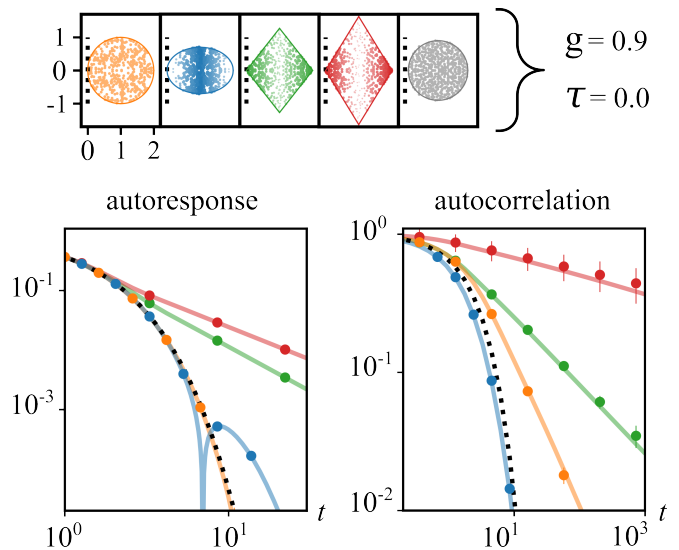


Figure 2. Same synaptic statistics correspond to different dynamics. Top: Various eigenvalue distributions, corresponding to different connectivities, which to leading order in the number of neurons share the same synaptic statistics. Specifically, $g = 0.9$ and $\tau = 0$ (Eq. (2)), corresponding to independently distributed synaptic strengths following Gaussian statistics. The eigenvalue distributions are plotted in the complex plane $k = 1 - \lambda$ and are nearly critical, touching the line of linear instability $k_x = 0$. The archetypal case of an exactly Gaussian connectivity with the same synaptic statistics is also shown in black. Bottom: Autocorrelation and autoresponse functions decay in time, colored accordingly. Despite sharing the same leading order synaptic statistics, the different connectivities feature different eigenvalue distributions, and thus correspond to very different network dynamics: the autocorrelation and autoresponse can either decay exponentially (blue, orange) or with power-laws with varying exponents (red, green). Curves: theory; markers: simulation; dotted, black line: known theory for the archetypal case of a Gaussian connectivity. Other parameters: For a given eigenvalue distribution, ν is fixed according to Eq. (6) and Eq. (7) so to have $g = 0.9$ and $\tau = 0$. Going from left to right in the top panel, $\nu = 0.49, 0.7, 0.52, 0.37$.

bution. Our findings on the synaptic strength statistics are discussed in more detail in Section IV.

III. EFFECT ON DYNAMICS

In this section, we characterize how the eigenvalue distribution affects the network dynamics. We focus on networks at criticality. This regime is of particular interest because of the wealth of characteristic features of criticality, like power-laws, that are experimentally observed in brain networks [3, 15, 16], feeding the so-called critical brain hypothesis [28]. For example, a power-law decay in the PC spectrum, whose observed fine-tuning [3] we want to describe in this work, only arises when the model (1) is close to criticality [11]. Theoretical studies also sug-

gest the edge of criticality as an optimal computational regime [29–31].

It is natural to consider the shifted eigenvalues $k \equiv \lambda - 1$, that is the eigenvalues of the dynamics' Jacobian $J - \mathbb{I}$. Thus, calling $k \equiv k_x + ik_y$, a mode has decay constant k_x and oscillation frequency k_y . The network is at the critical point when the eigenvalue distribution touches the line of linear instability $k_x = 0$ from the right (see e.g. Fig. 2, top). Occasionally, we parameterize a small distance away from criticality by adding a small leak term $-\delta \cdot x$ to the *rhs* of Eq. (1). This effectively shifts the eigenvalues of the Jacobian $k \rightarrow k + \delta$, so the longest living mode have decay constant δ , rather than 0.

The main result of this section is that the density of nearly critical eigenvalues controls various dynamical observables that are found to be fine-tuned in cortical networks, including the dimensionality and PC spectrum of neural activity. This happens thanks to a direct link between the density of nearly critical eigenvalues and the power-law scaling exponents characterizing these observables. Precisely, we show that these scaling exponents are algebraic functions of the exponents d or \bar{d} , controlling the density of nearly critical eigenvalues through $p(k_x) \stackrel{k \rightarrow 0}{\sim} k_x^{d-1}$ or $p(\rho) \stackrel{k \rightarrow 0}{\sim} \rho^{\bar{d}-1}$, where in the first case we consider the marginal distribution of the eigenvalues' real part k_x , while the second case describes the marginal distribution of the eigenvalues' radial component ρ , with $k \equiv \rho e^{i\phi}$. We call the exponent d the network's effective spatial dimension, in analogy with classical critical phenomena, as exposed later.

Note that, while here we focus on nearly critical systems, our theory works also away from criticality, showing qualitatively similar results. The difference is that, at the critical point, the effect of the eigenvalue distribution on the dynamics is more apparent and readily quantifiable in terms of power-law scaling exponents.

A. Autocorrelation and autoreponse

Before focusing on the dimensionality and PC component spectrum of neural activity, it is instructive to consider two other quantities commonly studied in disordered networks [25]: the population averaged autocorrelation and autoreponse functions. These help to illustrate the effect of the distribution of nearly critical eigenvalues on the dynamics. We show that these functions have a power-law decay in time, whose exponent is controlled by the density of nearly critical modes. Furthermore, we show that these power-laws only emerge for certain distributions of oscillation frequencies, which control a transition from exponential to power-law decay.

We define the population averaged autocorrelation as $A(t) = \frac{1}{N} \sum_i \langle x_i(t) x_i(0) \rangle_\xi$, and the population averaged autoreponse as $r(t) = \frac{1}{N} \sum_i \lim_{\epsilon \rightarrow 0} \frac{1}{\epsilon} \langle x_i^\epsilon(t) - x_i(t) \rangle_\xi$, where $x_i^\epsilon(t)$ is the neural activity if Eq. (1) is perturbed by a term

$\epsilon \delta(t)$ along direction i .

Standard linear response theory gives

$$r(t > 0) = \frac{1}{N} \sum_\alpha \exp(-k_\alpha t) \stackrel{N \rightarrow \infty}{\sim} \int \mathcal{D}k \exp(-kt), \quad (8)$$

where in the last step we have taken the limit of the sum of eigenvalues to an integral over their probability density, with integration measure $\mathcal{D}k \equiv p(k) dk$, valid for large N . In this limit, using our random matrix theory (see Appendix B and the Supplemental Material [32]), we find $A(t)$ has the expression

$$A(t) = \frac{1 + \nu^2}{1 - \nu^2} \int \frac{\mathcal{D}k}{2k_x} \exp(-k|t|) - \frac{2\nu^2}{1 - \nu^2} \int \frac{\mathcal{D}k_1 \mathcal{D}k_2}{k_1 + k_2} \exp(-k_1|t|). \quad (9)$$

The autoreponse $r(t)$ depends only on the eigenvalue distribution, and not on the eigenvectors. The autocorrelation $A(t)$ instead also depends on the eigenvectors' distribution, as reflected by the parameter ν . The first term in Eq. (9) is the only one present in the limit of a normal network $\nu \rightarrow 0$, while the second term reflects a non-vanishing overlap between eigenvectors in the non-normal case (see Appendix B). For reference, we also report the known expression for the archetypal choice of a Gaussian connectivity, in the $\tau = 0$ case: $r(t > 0) \stackrel{\delta \rightarrow 0}{\sim} \exp(-t)$ and $A(t) \stackrel{\delta \rightarrow 0}{\sim} \frac{D}{4\delta} \exp(-\delta t)$.

Before looking at the time dependence of $r(t)$ and $A(t)$, it is instructive to focus on the equal-time variance $A(0)$, so as to introduce the concept of the network's effective spatial dimension. As for the archetypal choice of J , the variance can diverge as we approach criticality $\delta \rightarrow 0$. It's divergent behavior near criticality is described by the exponent d characterizing the density of nearly critical modes

$$p(k_x) \stackrel{k_x \rightarrow 0}{\sim} k_x^{d-1}. \quad (10)$$

Indeed, we note that, when the variance diverges, the first term in Eq. (9) dominates, behaving like

$$\sim \int \frac{p(k_x) dk_x}{k_x + \delta} \sim \int \frac{k_x^{d-1} dk_x}{k_x + \delta} \propto \begin{cases} \delta^{d-1} & d < 1 \\ \text{const} & d > 1 \end{cases}, \quad (11)$$

where we introduced a small distance δ from criticality. We can see that the variance remains finite for $d > d_0 = 1$, while it diverges for smaller d .

Note that an analogous expression to Eq. (11) can be found for the variance of classical critical phenomena [33–35], with d playing the role of the system's spatial dimension. In fact, for a very special choice of J , Eq. (1) becomes the stochastic heat equation, a linear model of reference for out of equilibrium critical phenomena [34, 35]. Specifically, one needs to choose J such that $J - \mathbb{I}$ implements a discretization of the Laplace operator

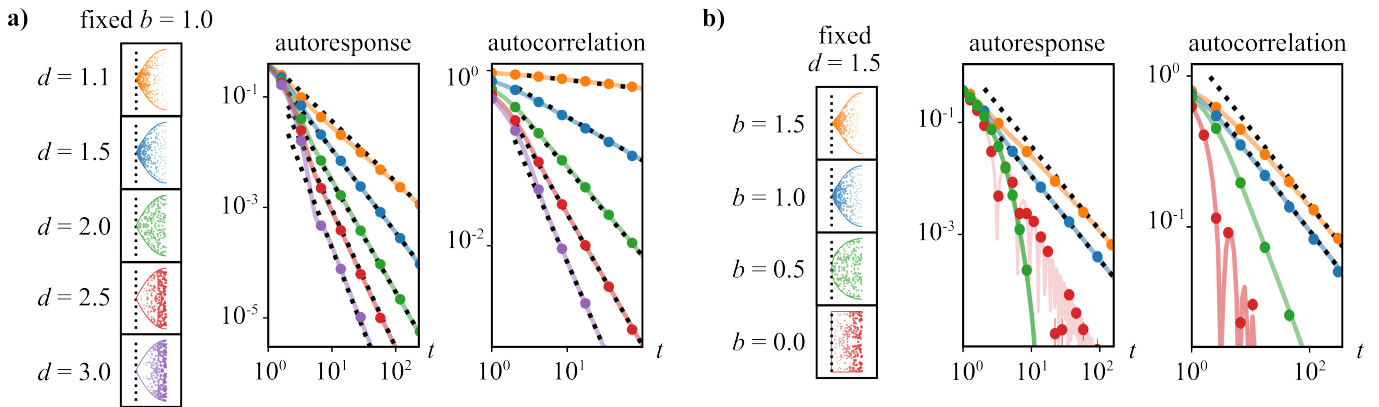


Figure 3. (a) Power-law decay, controlled by the density of nearly-critical eigenvalues. On the left, different distributions of nearly critical eigenvalues are shown in the k_x - k_y plane for fixed $b = 1$ and varying d . The dashed vertical line represents the critical line of instability at $k = 0$. Corresponding decay in time of the autoresponse $r(t)$ and normalized autocorrelation $A(t)/A(0)$, colored accordingly. Solid curves: theory; markers: simulations; dashed, black lines: power-law decay with exponent d for the autoresponse and $d - 1$ for the autocorrelation. (b) Transition from power-law to faster decay, controlled by the distribution of oscillation frequencies. The autoresponse and normalized autocorrelation are shown for fixed $d = 1.5$ and varying b . Solid curves: theory; markers: simulation. For $b \geq 1$, we see a power law decay (dashed, black lines) with exponent fixed by the value of d , regardless of the value of b . For $b < 1$ the decay is faster. Other parameters: $N = 10^2$, $\nu = 1/\sqrt{3}$.

(i.e. the kinetic term) on a d -dimensional lattice. Then, the connectivity eigenmodes become a very specific set of modes: the Fourier modes, with associated wave-vector \vec{k} . The density of nearly critical Fourier modes is fixed to be $p(\|\vec{k}\|) \sim \|\vec{k}\|^{d-1}$, where d cannot take arbitrary values as in a generic network, but corresponds to the system's spatial dimension. In analogy, we call d the network's effective spatial dimension. A difference between networks and classical systems is that d can take a continuous, rather than discrete range of values, thanks to all possible shapes of the connectivity's eigenvalue distribution. As in classical critical phenomena, we will see how d controls the scaling laws of dynamical observables.

Having introduced the network's effective spatial dimension, we shall now focus on the asymptotic long-time dependence of $r(t)$ and $A(t)$. As for $A(0)$, this is naturally characterized by the marginal distribution $p(k_x)$ of decay constants of nearly critical modes, through the exponent d . In addition, the conditional distribution of oscillation frequencies $p(k_y|k_x)$ for a given decay constant is now important. We find this quantity to control whether the decay in time is power-law or exponential. Differently than for $A(0)$, a characterization for a generic $p(k_y|k_x)$ is hard in this case. To enlighten the role of oscillation frequencies, we consider the case of a uniform distribution of oscillation frequencies

$$p(k_y|k_x) \propto \theta(B(k_x) - |k_y|), \quad B(k_x) \stackrel{k_x \rightarrow 0}{\sim} k_x^b. \quad (12)$$

As illustrated in Fig. 3, two exponents parameterize the scaling properties of the distribution of nearly critical modes. Exponent d parameterizes the scaling of the density of nearly critical modes Eq. (10), while exponent b parameterizes the scaling of the maximum oscillation

frequency of nearly critical modes $|k_y|_{max} \propto k_x^b$, i.e. the boundary of the eigenvalue distribution. We find that these exponents also characterize the dynamics in a very direct way, as illustrated in Fig. 3. Exponent b controls how the autocorrelation and autoresponse decay in time (Fig. 3(b)). In particular, it determines a transition from a power-law decay to a faster decay: for slow enough oscillations of nearly critical modes ($b \geq 1$) we have the power-law decay; when oscillations are too fast ($b < 1$), instead, the decay is slower, potentially exponential and oscillating. Exponent d controls the power-law exponent in the case of exponential decay (Fig. 3(a)): $r(t) \sim t^{-d}$ and $A(t) \sim t^{-(d-1)}$.

Considering $r(t)$ as an example, this can be easily seen by integrating Eq. (8) over k_y and passing to the dimensionless variable $p \equiv k_x t$, obtaining

$$r(t) \stackrel{t \rightarrow \infty}{\sim} \frac{1}{t^{a+2}} \int_0^\infty dp p^a \exp(-p) \sin(p^b t^{(1-b)}). \quad (13)$$

We can see that, if $b > 1$, oscillations are unimportant in the long-time limit, as we can expand the oscillating term $\sin(x) \sim x$ in the integrand, recovering the power-law scaling $r(t) \sim t^{-d}$. If $b < 1$, instead, oscillations interfere with the build up of nearly critical modes into a pure power law. The reasoning is completely analogous for $A(t)$, noting that the first term in Eq. (9) dominates in the long-time limit. This means that, though the degree ν of non-normality of the network affects quantitatively $A(t)$, it does not affect its power-law decay exponent (see Fig. C1).

Note that in the archetypal case of a Gaussian connectivity, the decay of both $r(t)$ and $A(t)$ is known to be exponential. The emergence of power-laws is a novelty of certain connectivities here considered, whose nearly

critical modes have sufficiently slow oscillation frequencies ($b > 1$). This phenomenon may help accounting for the emergence of power-laws ubiquitously observed in cortical networks, both in correlation functions [15], and in the network's response, as in neural avalanches [14, 16, 36]. Of particular interest for neural avalanches is the here discovered ability of connectivity to continuously vary the system's dynamical scaling exponents, in line with the recently observed variability in avalanche power-law exponents [16], and in contrast with the classical notion of exponents being determined by the universality class alone. While we leave investigating neural avalanches to future work, we note that this variability may be explained here by a fluctuation in the network's operational point, causing a fluctuation in the network's effective connectivity, thus in the distribution of nearly critical eigenvalues controlling power-law exponents.

We conclude remarking that the power-law scaling found in this section, as well as in the following sections, only depends on a very generic property of the eigenvalue distribution, namely the scaling Eq. (10). Other properties of the eigenvalue distribution can affect quantitatively the shape of $A(t)$ and $r(t)$, but are irrelevant with regards to the power-law scaling. For example, Fig. 3(b) (cases $b = 1.0, 1.5$) illustrates how varying the shape of the distribution boundary, here controlled by b , does not affect the power-law exponents, which is fixed by d . We further exemplify this in Fig. C1. For example, we also show how the power-law scaling is not altered by a stretching of the eigenvalue distribution along the imaginary axis (cf. Eq. (A1)). By Eq. (7), this alters the degree of symmetry τ of the connectivity matrix. Thus, in particular, also symmetry does not affect the power-law decay exponent.

B. Dimensionality

In this subsection we characterize the effect of the density of nearly critical eigenvalues on the dimensionality of neural activity. Recent research has shown the high relevance of this measure for neural computation [3, 7, 8, 37]. Dimensionality indeed appears to be optimized into both a low [4–6] and high [3, 7] dimensional regime, depending on the cortical area and its specific computational tasks. Here we show how the density of nearly critical eigenvalues can flexibly tune dimensionality across both regimes, thanks to a novel transition between high and low dimensional activity.

Dimensionality is typically defined through the principal components spectrum of the neuronal activities' covariance matrix. Here we consider both the case of the equal-time covariance $C_{ij} = \langle x_i(t)x_j(t) \rangle$ and the long time-window covariance $C_{ij} = \lim_{T \rightarrow \infty} \frac{1}{T} \langle \hat{x}_i(0)\hat{x}_j(0) \rangle$, where we defined the Fourier transformed neural activity $\hat{x}_i(\omega) = \int_{-\frac{T}{2}}^{\frac{T}{2}} dt e^{-i\omega t} x_i(t)$. The so-called principal components of the covariance matrix are its eigenmodes,

defined through the decomposition

$$C = \sum_{\alpha} U_{\alpha} c_{\alpha} U_{\alpha}^T, \quad (14)$$

with the eigenvectors U_{α} identifying orthogonal directions of neuronal variability, and the eigenvalues $c_{\alpha} \geq 0$ its intensity along that direction. Dimensionality is an estimate of how many of the strongest principal components are required to explain most of neuronal variability. A commonly adopted measure of dimensionality is the participation ratio [11, 12]

$$D \equiv \frac{(\sum_{\alpha} c_{\alpha})^2}{\sum_{\alpha} c_{\alpha}^2} = \frac{(\text{Tr}[C])^2}{\text{Tr}[C^2]}, \quad (15)$$

which can conveniently be reduced to traces of powers of the covariance matrix. The latter we are able to compute with our random matrix theory (see Appendix B and the Supplemental Material [32]). We now proceed to characterize the behavior of dimensionality near criticality.

1. Equal time covariance

Let us start considering the equal-time covariance. Once again, we find that dimensionality is controlled by the density of nearly critical modes Eq. (10) through the exponent d . The full expression for the dimensionality is made intricate by its dependence on the degree ν of non-orthogonality, and is given in the Supplemental Material [32]. However, we can get a readily interpretable picture of its dependence on d by looking at the asymptotic behavior at criticality ($\delta \rightarrow 0$). Note the numerator in Eq. (15) corresponds to $A(t=0)^2$ given in Eq. (9). We already discussed its diverging behavior near criticality in Eq. (11). The full expression for the denominator $\text{Tr}[C^2]$ is lengthy and is reported in the Supplemental Material [32]. The expression is analogous to Eq. (9), containing a first term surviving for $\nu \rightarrow 0$, which is the one dominating the divergent behavior near criticality, in addition to terms due to the network non-normality, analogous to the second term in Eq. (9). The dominating term behaves as

$$\sim \int \frac{p(k_x) dk_x}{(k_x + \delta)^2} \sim \int \frac{k_x^{d-1} dk_x}{(k_x + \delta)^2} \propto \begin{cases} \delta^{d-2} & d < 2 \\ \text{const} & d > 2 \end{cases}. \quad (16)$$

Combining Eq. (11) and Eq. (16) into Eq. (15), we therefore distinguish the behavior of dimensionality into three regions (Fig. 4(a)): for $d > 2$, we are in a high-dimensional regime, in which dimensionality is finite even at criticality; for $1 < d < 2$ we have low-dimensional activity, decaying as δ^{2-d} ; for $d < 1$ again we have low-dimensional activity, but decaying as δ^d . We therefore have a transition from high to low dimensional activity at $d = 2$. The transition becomes infinitely sharp at criticality. Otherwise, dimensionality forms a bell shape in the low-dimensional regime $d < 2$, with an optimum for

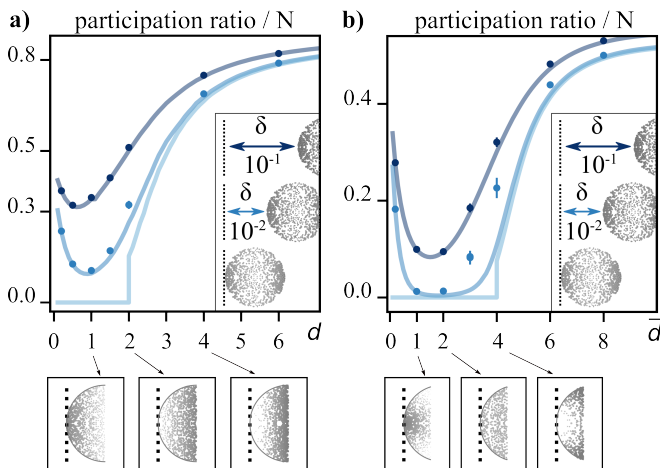


Figure 4. Transition from high to low dimensionality, controlled by the density of nearly critical eigenvalues. (a) participation ratio for the equal-time covariance, as a function of d . Curves in lighter blue correspond to decreasing values of δ (see inset). Solid curves: theory; markers: simulation. Only theory is shown for $\delta = 0$ (lightest blue), at which the transition is infinitely sharp. At the bottom, distributions of nearly critical eigenvalues are shown for some example values of d . (b) is analogous to (a), showing the participation ratio for the long time-window covariance as a function of \bar{d} . Note an eventual offset between theory and simulation for the smaller δ is due to finite size effects (see Fig. S1 in the Supplemental Material [32]). Other parameters: (a) $N = 10^3$, $\nu = 1/\sqrt{3}$, $b = 0.5$; (b) $N = 8 \cdot 10^3$.

connectivities with dimension $d \sim 1$, at which the dimensionality of the input noise is reduced the most. This last observation may also be interesting for initializing the connectivity of artificial networks at an optimal starting point for dimensionality reduction, from which to begin the network training. Note how the asymptotic description we have just given well describes the full analytical expression for the dimensionality even further away from criticality, e.g. for $\delta = 0.1$.

Once again, we show in Fig. C1 that both the degree of non-normality and other details in the shape of the eigenvalue distribution do not affect qualitatively our predictions.

2. Long time-window covariance

For the long-time window covariance the reasoning is completely analogous. Integrals of the same kind as Eq. (11) appear (see Appendix B). The main difference is that, while in Eq. (11) the relevant direction of integration approaching the critical point $k = 0$ was the one along the real axis k_x , for the long-time window covariance, instead, the relevant direction is the radial one ρ , where we defined $k \equiv \rho e^{i\phi}$. We therefore introduce a radial dimension \bar{d} controlling the density of nearly critical

modes along the radial direction

$$p(\rho) \stackrel{\rho \rightarrow 0}{\sim} \rho^{\bar{d}-1}. \quad (17)$$

The results are then completely analogous to those for the equal-time covariance, and are shown in Fig. 4(b). In this case, the transition between high and low dimensionality occurs at $\bar{d} = 4$. In the low-dimensional regime, dimensionality is $\sim \delta^{4-\bar{d}}$ for $2 < \bar{d} < 4$, and $\sim \delta^{\bar{d}}$ for $\bar{d} < 2$. The optimum is at $\bar{d} = 2$.

Note that, in the archetypal case of Gaussian J , we are in the low-dimensional regime and dimensionality decays as δ^2 [11, 12, 24]. This is reproduced also for our matrix with a matching distribution of eigenvalues (i.e. uniform on the circle), which has radial dimension $\bar{d} = 2$. Going beyond, here we show that with different shapes of the eigenvalue distribution, any other scaling behavior can be obtained. In practice this implies that, through connectivity, dimensionality can be flexibly tuned within a wide range of values (cf. Fig. 4). Most importantly, also a high-dimensional regime can be accessed, in which dimensionality remains finite even at the critical point. This is of relevance because other connectivity structures like second order motifs can only control dimensionality within the low-dimensional regime, when at criticality [11, 12]. In the density of nearly critical eigenvalues, instead, we have identified a connectivity structure that can flexibly tune dimensionality across the entire range of low and high dimensional activity which is observed throughout cortex [3–7]. The ability to control dimensionality while staying at the critical point is important in the light of the ubiquitous evidence of criticality found in brain dynamics [28], in particular the characteristic presence of power-laws [3, 14–16], such as, for example, that in PC spectrum [3] discussed below.

C. Principal components spectrum

Another dynamical observable that has recently received considerable interest is the PC spectrum of neural activity, i.e. the full set of PC eigenvalues c appearing in Eq. (14), plotted from largest to smallest. For example, a recent experimental study has considered the PC spectrum of neural activity in V1 of mice, during the encoding of image stimuli [3]. A power-law decay with exponent $\alpha = 1$ is found, which is theoretically argued to be optimal for encoding visual stimuli: larger α would correspond to fewer details encoded, while a smaller α would be too sensitive to details and correspond to a fractal representation. This optimal exponent has also been found in artificial recurrent networks trained to perform image classification [38]. Recent theoretical work has derived a similar power-law decay for a network governed by Eq. (1), for the archetypal choice of J [11]. There, the power-law exponent is $\alpha = 1.5$, different from the one experimentally observed. Furthermore, it is shown that no second order motif structure can alter this exponent. Here we show how the density of nearly critical

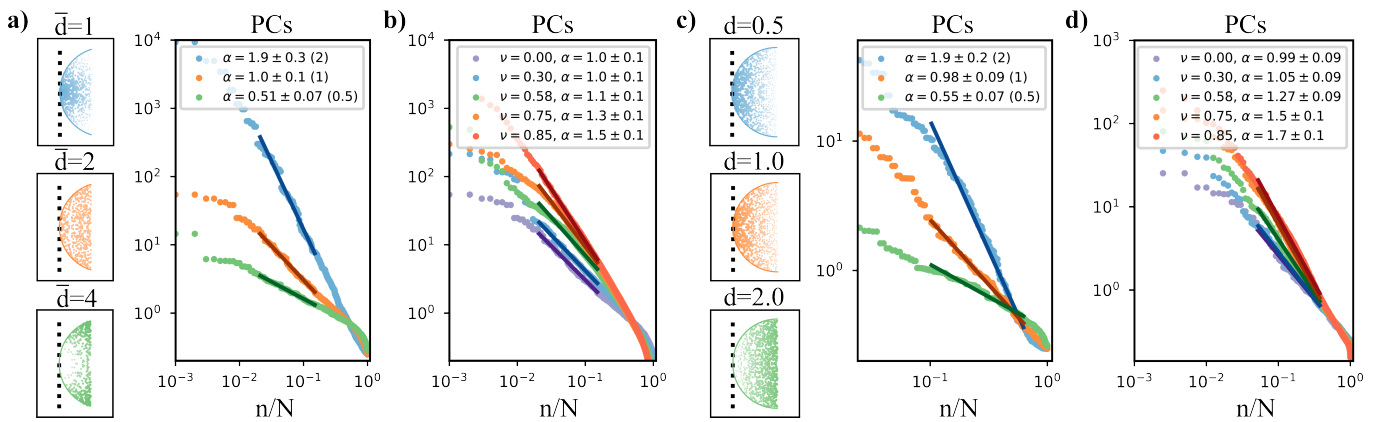


Figure 5. The density of nearly critical eigenvalues controls the slope of the PC spectrum. PC spectrum plotted against the fractional rank n/N . (a-b) Case of the long time-window covariance. (a) Case $\nu = 0$. Shown for varying densities of nearly critical eigenvalues, parameterized by \bar{d} (shown on the left and colored accordingly). Markers: simulation; lines: fitting power-law; legend: mean and standard deviation of the power law exponent α , found for 48 independent realizations of the connectivity. Theoretical prediction in parenthesis. (b) Same as (a), but for fixed $\bar{d} = 2$ and varying ν (see legend). (c-d) Same as (a-b), but for the case of the equal-time covariance: In (c) we fix $\nu = 0$ and vary d ; In (d) we fix $d = 1$ and vary ν . Other parameters: (a-b) $N = 10^3$, $\delta = 0.01$, $b = 0.5$; (c-d) $N = 4 \cdot 10^2$, $\delta = 0.01$.

eigenvalues can instead control this exponent, thus identifying a connectivity structure that can account for the experimental observation of an optimized PC spectrum.

Deriving an expression for $p(c)$ for any value of the degree of non-normality ν is a hard task that we leave for future work. However, we can easily derive $p(c)$ for the normal case $\nu = 0$, and study numerically what happens for $\nu \neq 0$.

Let us first consider the principal components of the time integrated covariance. For $\nu = 0$, the principal components eigenvalues c are simply related to the connectivity eigenvalues $k = \rho e^{i\phi}$ by $c = \rho^{-2}$ (see Appendix B). Therefore, $p(c) = p(\rho(c)) c^{-\frac{3}{2}}$. Once again, we see that a power-law emerges, that is controlled by the density of nearly critical modes Eq. (17): $p(c) \stackrel{c \rightarrow \infty}{\sim} c^{-\frac{\bar{d}+2}{2}}$. It follows that the power-law decay of c with its rank n is $c \sim n^{-\alpha}$, with $\alpha = 2/\bar{d}$. Therefore, as illustrated in Fig. 5(a), varying the connectivity's density of nearly critical modes tunes the power-law decay of the principal components spectrum. Numerically, we find that also the degree of non-normality ν can partially control the decay exponent. As illustrated in Fig. 5(b), for a fixed \bar{d} , increasing ν increases the exponent α . This effect is weak for small or intermediate values of ν , and starts becoming apparent for large values of ν . Finally, let us note that a uniform elliptical eigenvalue distribution corresponds to $\bar{d} = 2$ and therefore to $\alpha = 1$ in our ensemble. This is different from the value $\alpha = 1.5$ found for the archetypal J , which has the same eigenvalue distribution. The difference is caused by the different statistics for the eigenvectors, which in the archetypal case are strongly non-orthogonal and correlated to the eigenvalues. Interestingly, the exponent $\alpha = 1.5$ is approached in our case by increasing ν to higher degrees of non-normality $\nu \sim 0.85$. We characterize the strongly

non-normal regime in IV C, finding a similar qualitative dependence of α on \bar{d} . In particular, the mechanism by which the density of nearly critical eigenvalues can fine-tune the slope of the PC spectrum is preserved also in this regime.

As illustrated in Fig. 5(c-d), completely analogous results follow for the equal-time covariance. The only difference is that here $c = k_x^{-1}$ (see Appendix B), thus the power-law exponent α is still controlled by the density of nearly critical modes Eq. (10), but the one obtained approaching the critical point along the real axis. Specifically, we have a power-law decay with rank $c \sim n^{-\alpha}$, with $\alpha = 1/d$.

IV. CONNECTIVITY STATISTICS

In this section, we present in more detail our results deriving the synaptic strength statistics of the connectivity matrices in our ensemble.

A. Leading order synaptic statistics

First, we comment on the leading order synaptic statistics. To leading order, the connectivity is Gaussian and presents only reciprocal motifs, just as in the archetypal case. The synaptic strength statistics are given by Eq. (6) and Eq. (7). These expressions depend on both the degree of non-normality ν and the second moments of the eigenvalue distribution.

Let us first fix ν and discuss the effect of the eigenvalue distribution. Notice the synaptic gain g is controlled by the overall spread of eigenvalues on the complex plane. Unsurprisingly, increasing the spectral radius

of the eigenvalue distribution corresponds to proportionally increasing the synaptic gain.

The degree of symmetry τ is instead controlled by the relative spread of the distribution along the real and imaginary axes. Notice that Eq. (7) generalizes to any eigenvalue distribution in our ensemble a fact that could already be observed for the elliptical distribution corresponding to the archetypal J : there, varying τ corresponds to stretching the ellipse along the imaginary or real axis (see e.g. Fig. 1). In fact, provided we choose $\nu^2 = \frac{1-\tau^2}{3+\tau^2}$, our ensemble reproduces the values of g and τ of the archetypal connectivity, when it is initialized with the same elliptical eigenvalue distribution. For the special case $\tau = 0$, we have to choose $\nu = 1/\sqrt{3} \sim 0.577$ (see Fig. 6(a)). Note, however, that the connectivities in the two ensembles are still different: On the one hand, synaptic strength statistics of our ensemble have a more complicated subleading order structure, which accounts for the different possible shapes of the eigenvalue distribution. On the other hand, the archetypal connectivity has strongly non-orthogonal eigenvectors and a fine-tuned correlation structure between eigenvalues and eigenvectors, which we introduce in our analysis later in IVC.

For a fixed eigenvalue distribution, notice g and τ can still be partially tuned by the degree of non-normality ν . For example, stronger normality of the network (i.e. smaller ν) corresponds to stronger (anti)symmetry. Note that, as should be expected, perfect (anti)symmetry is only achieved in the special limit of a normal network $\nu = 0$ and an eigenvalue distribution collapsed on the (imaginary) real axis.

Regarding the effect of ν on the synaptic gain g , note that this remains of $\mathcal{O}(1)$ for considerably strong $\nu \sim 0.9$ (Fig. 6(a)). However, a too strong non-normality $\nu \rightarrow 1$ makes g diverge. More extreme degrees of non-normality require correlations between eigenvalues and eigenvectors, in order to keep g of order unity. We discuss this case in IVC. Finally, note that this divergence of the synaptic gain is a non-trivial effect of the eigenvectors' non-orthogonality. It occurs for any fixed spectral radius of the eigenvalue distribution. In particular, it cannot be compensated by a trivial rescaling of the synaptic strengths, as this would also shrink the spectral radius.

B. Hidden synaptic structures

Despite the connectivity being Gaussian to leading order in N , it still contains all sorts of higher order statistics. These are expected, as they must account for all eigenvalue distributions that are possible within our ensemble. The surprising result that we show here, however, is that these higher order statistics appear only at subleading order in N .

Writing the connectivity in dimensionless units $\bar{J} := J\sqrt{\frac{N}{g}}$, we prove (see Appendix A5 and the Sup-

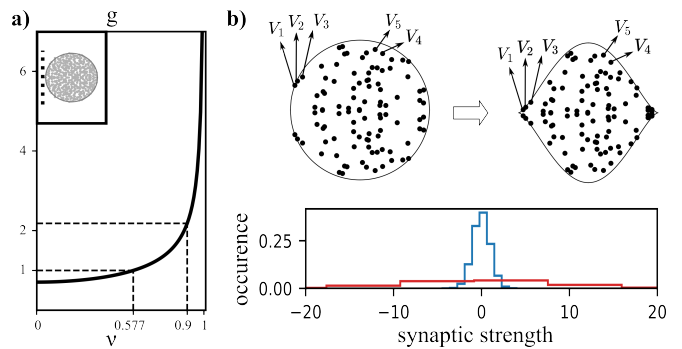


Figure 6. (a) Synaptic gain g as a function of the degree of non-normality ν , for the case of a uniform circular distribution (inset), as that found in the archetypal connectivity for $g = 1$ and $\tau = 0$. The dotted lines highlight the special value $\nu = 1/\sqrt{3} \sim 0.577$, for which $g = 1$ is recollected. Also the value $\nu = 0.9$ is highlighted, for which g is still of $\mathcal{O}(1)$. (b) Method for initializing connectivities with arbitrary eigenvalue distribution in the strongly non-normal regime. Top: starting from the archetypal Gaussian connectivity, we continuously shift its eigenvalues (left) into a new distribution (right). Each eigenvector remains associated to the original eigenvalue, so as to preserve the tight correlation structure that ensures $g = \mathcal{O}(1)$. This can be checked in the blue histogram of scaled synaptic strengths $\sqrt{N}J_{ij}$ at the bottom, which has an $\mathcal{O}(1)$ variance. If instead the strongly non-normal eigenvectors were randomly assigned to the eigenvalues of the new distribution, we would have a divergent synaptic gain (red histogram).

plemental Material [32]) that higher order cumulants $\langle\langle \bar{J}_{i_1 i_2} \dots \bar{J}_{i_{2n-1} i_{2n}} \rangle\rangle$ are of order $\mathcal{O}\left(\frac{1}{\sqrt{N}}\right)$ for $n = 3$ and of order $\mathcal{O}\left(\frac{1}{N}\right)$ for any other $n > 3$. We also prove that the only nonvanishing cumulants are those for which all indices i_1, \dots, i_{2n} are matched in pairs. For second order cumulants, this means only reciprocal motifs, associated with the cumulant $\langle\langle J_{ij} J_{ji} \rangle\rangle$, are present. For example, instead, cumulants like $\langle\langle J_{ij} J_{jk} \rangle\rangle$, $\langle\langle J_{ji} J_{jk} \rangle\rangle$ or $\langle\langle J_{ij} J_{jk} \rangle\rangle$, associated respectively with divergent, convergent, or chain motifs are null (see Fig. 1 for a schematic representation). For a numerical validation of our predictions on the synaptic strength statistics, see Fig. C2 and Fig. S6 in the Supplemental Material [32].

The above results show that the here studied eigenmode structures remain hidden to an analysis of local connectivity motifs. Indeed, different shapes of the eigenvalue distribution and different degrees of the eigenvectors' non-orthogonality are in large part not reflected by motif structures. In particular, only the second order statistics of the eigenvalues distribution affect the synaptic strength statistics, through Equations (6) and (7). All other details about the shape of the eigenvalue distribution remain hidden in correlations that are vanishingly small in the number of neurons. In particular, details like the density of nearly critical eigenvalues, which we have shown in Section III to significantly control network dynamics, remain hidden (cf. Fig. 2). Note that

this does not imply that these eigenmode structures are undetectable – in fact, they are clearly revealed by an eigenmode analysis of connectivity, for example through different shapes of the eigenvalue distribution. What this result shows is that these structures are intrinsically collective: they cannot be reduced to any local connectivity pattern, but rather involve all connections concertedly.

These observations also provide a new insight into the paradox of structure within randomness in highly heterogeneous circuits. We have indeed shown that there can be much structure encoded in the eigenmode statistics of an apparently random connectivity, which remains hidden within the synaptic strength statistics. This opens new possibilities for modeling neural networks: these eigenmode structures correspond to additional degrees of freedom which can be appropriately specified, without affecting other experimentally observed parameters, which are traditionally fixed in connectivity models. For example, as illustrated in Fig. 2, the density of nearly critical eigenvalues can be specified without affecting the variance of synaptic strengths or the abundance of reciprocal motifs. Other second order motifs are also unaffected, as these are represented by additive low rank perturbations to the here studied bulk connectivity [11]. From the opposite angle, fixing these traditional parameters does not fix the density of nearly critical eigenvalues. Rather, for the typical choice of a Gaussian connectivity, it selects the specific case of a uniform elliptical eigenvalue distribution. Given its impact on the dynamics, however, the density of nearly-critical eigenvalues could instead be fixed using our theory, so to match experimentally observed power-law exponents, for example those found in the PC spectrum of neural activity, in the case of V1.

C. Strongly non-normal regime

In this subsection we numerically extend our analysis to the case of strongly non-orthogonal eigenvectors. With this extension, our analysis encompasses the case of the archetypal choice of Gaussian connectivity. We will see that most results obtained in Section III qualitatively apply also to this regime.

In IV A we noticed that the synaptic gain g diverges in the strongly non-normal regime $\nu \rightarrow 1$. In Appendix A 2 we give an intuition for this divergence in terms of the eigenvalues of the eigenvector matrix. Here we rather focus on giving an intuition on how g can be kept of $\mathcal{O}(1)$ even in this strongly non-normal regime, and provide a method to explore this regime numerically.

It is instructive to inspect the archetypal Gaussian connectivity. This has $g = \mathcal{O}(1)$, while at the same time presenting strongly non-orthogonal eigenvectors (see Fig. S2 (a) in the Supplemental Material [32]). This is made possible by a fine-tuned correlation structure between eigenvalues and eigenvectors, which we do not have in our original ensemble. We can see this by randomly shuffling the association between eigenvectors and eigenvalues and

then reconstruct the connectivity through Eq. (3): the synaptic gain then diverges with N , just like it does in our ensemble, in which no correlation structure is assumed (see Fig. S2 (b-c) in the Supplemental Material [32]). This shows that the original association was fine-tuned to tightly balance the summation on the r.h.s. of Eq. (3) to result in finite synaptic strengths.

Leveraging on these insights, we devise a method to initialize connectivities also in this strongly non-normal regime, while still allowing for any shape of the eigenvalue distribution. The idea is to preserve the necessary correlation structure found in the archetypal connectivity, even when choosing an eigenvalue distribution different than uniform elliptical. The method’s details are given in Appendix A 4. The idea can be summarized as follows (Fig. 6(b)): We start from the archetypal J for $\tau = 0$, which naturally implements strongly non-normal eigenvectors and the necessary correlations with eigenvalues. It’s eigenvalue distribution will be uniform on the circle. We obtain other eigenvalue distributions by continuously shifting the eigenvalues into some new position in the complex plane, such that they are distributed according to the new desired distribution. The intuition is that the continuous shift preserves to some extent the tight correlations between eigenvalues and eigenvectors, such that the connectivity remains well defined even if the eigenvectors are strongly non-orthogonal. We verify numerically that indeed this method ensures a well defined $g = \mathcal{O}(1)$ (see Fig. 6(b) and Fig. S2 in the Supplemental Material [32]). We call the ensemble of connectivities obtained with this method the *strongly non-normal ensemble*, and refer to the ensemble discussed in the rest of the manuscript, for which we derived analytical predictions, as the *original ensemble*.

Our numerical simulations for the strongly non-normal ensemble show that our theory developed for the original ensemble still qualitatively captures most of the phenomena described in Section III. As shown in Fig. 7(a-b), dimensionality as a function of the density of nearly critical modes, as parameterized by d or \bar{d} , presents a similar shape as that shown in Fig. 4. As could be expected, it is for strong degrees of non-normality that our theory for the original ensemble is most similar to the here presented simulations. Fig. S3 in the Supplemental Material [32] shows additional simulations further away from criticality.

As can be seen in Fig. 7(c-d), d or \bar{d} also control the power-law decay exponent of the principal components spectrum. As we already noted in III C, the decay is steeper than in our original ensemble at $\nu = 0$, but is in fact very similar to our original ensemble at large ν .

For the autoresponse function, the results are exactly the same as those for the original ensemble, as this function does not depend on the eigenvector statistics. The only different behavior is shown by the autocorrelation function (see Fig. S4 in the Supplemental Material [32]). There, we find the autocorrelation to diverge in both its amplitude $A(0)$ and exponential decay time as $\delta \rightarrow 0$,

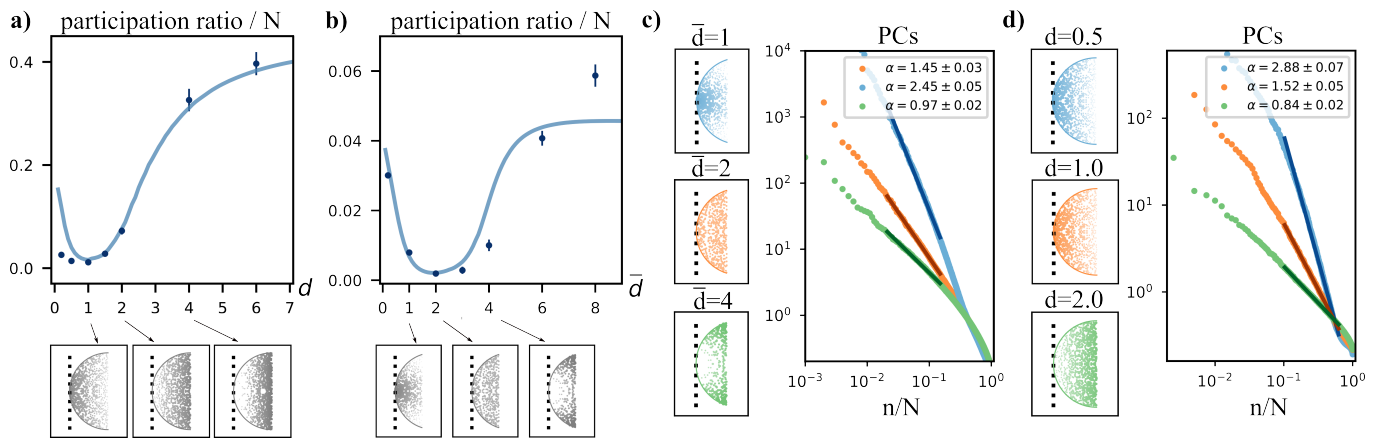


Figure 7. Strongly non-normal ensemble. (a-b) are analogous to Fig. 4(a-b), while (c-d) are analogous to Fig. 5(a) and Fig. 5(c). The same eigenvalue distributions are considered, but with strongly non-orthogonal eigenvectors. (a-b) participation ratio of the equal-time (a) and long time-window (b) covariance. $\delta = 0.01$. Markers: simulation. Solid line: theory for the original ensemble at $\nu = 0.8$ (a) and $\nu = 0.9$ (b), shown for comparison. (c-d) Principal components spectrum for the long time-window (c) and equal-time (d) covariance.

even for $d > d_0$ (cf. Eq. (11)). Moreover, regardless of the value of b , the decay is always exponential, rather than power-law. This suggests that, in the case of the autocorrelation, the interplay between strong non-orthogonality and correlations between eigenvalues and eigenvectors has a role that is not qualitatively captured by our original ensemble.

Not only the dynamics, but also the motifs statistics of these strongly non-normal connectivities appear to be qualitatively captured by our theory for the original ensemble (see Fig. C2 and Fig. S6 in the Supplemental Material [32]). In particular our simulations suggest that, also in this case, hidden synaptic structures control the shape of the different eigenvalue distributions and hence the different dynamics.

V. DISCUSSION

A fundamental quest of neuroscience is to identify the connectivity structures that underlie the observed fine tuning of neural activity into computationally optimal states. For cortical microcircuits, whose connectivity is highly heterogeneous, the challenge is often to identify these structures within an apparent randomness, that is in the connectivity statistics. Within this setting, the literature has mainly focused on the statistical abundance of local structures, such as connectivity motifs [10–13]. However, despite their impact on neural activity, for example its dimensionality [10, 12], there still remain many computationally relevant observables of network dynamics which cannot be controlled by these structures alone.

Here we discover another type of connectivity structures which can fine-tune such dynamical observables. These structures are of a complementary and fundamentally different nature than motifs: they are *collective*,

rather than *local*, and are encoded in the connectivity’s eigenmode statistics. We develop a novel random matrix theory that allows imposing these eigenmode structures on the connectivity, such as the shape of the eigenvalue distribution and the degree of the eigenvectors’ non-orthogonality, enabling us to systematically explore their effect on network dynamics. In particular, we find the density of nearly-critical eigenvalues to control dynamical observables that are found to be fine-tuned in brain networks, and whose optimization remained so far inaccessible to motif structures.

A. Structures controlling dynamics

Specifically, we show in III C that the slope of the PC spectrum of neural activity can be controlled in a continuous fashion. In particular, it can be fine-tuned into an optimal value for stimulus encoding, as observed in V1 of mice [3]. This functionally relevant feature of the PC spectrum is not controllable by any type of second order motifs [11]. Furthermore, we show in III B that dimensionality can be flexibly tuned across the entire range of low and high dimensional activity, even when the network is kept at criticality. This can happen thanks to a novel transition between low and high dimensional activity discovered in this manuscript, which is controlled by the density of nearly critical eigenvalues. In contrast, second order motifs can only control dimensionality within the low dimensional regime, when the network is critical [12]. Identifying a connectivity structure with such a broad and flexible control of dimensionality is important to account for the observation of both high [3, 7] and low [4–6] dimensional activity in different cortical areas [8], which are thought to select either of the two regimes to optimize their area-specific functions. Con-

trolling dimensionality while staying at the critical point is important in the light of the ubiquitous evidence of criticality found in brain dynamics [28], in particular the characteristic presence of power-laws [3, 14–16], such as, for example, that in PC spectrum [3] discussed above.

The novel mechanisms described above are here formulated in terms of a solid mathematical theory linking power-law exponents, ubiquitously observed in brain dynamics [3, 14–16], and connectivity. As we show in III A, the power-law scaling exponents of dynamical observables are directly related to the scaling exponent parameterizing the density of nearly critical eigenvalues, in analogy to how the system’s spatial dimension controls scaling in classical critical phenomena. Similar analogies had been previously restricted to symmetric networks [39–41], thus limiting their application to neuroscience, which needs to consider brain networks’ asymmetric connections. The latter case presents new technical challenges, such as non-orthogonal eigenvectors and complex eigenvalues, that are here tackled by a novel kind of random matrix theory.

Regarding complex eigenvalues, we find them to give rise to new phenomena specific to the asymmetric case: As we show in III A, the distribution of oscillation frequencies (i.e. the eigenvalues’ imaginary part) controls a transition from exponential to power-law decay of the autocorrelation and autoreponse functions. The emergence of power-laws in the asymmetric case is in particular a novelty of certain connectivities here considered, which may be relevant for describing neural avalanches in disordered networks (cf. III A).

Regarding the eigenvectors’ non-orthogonality, we find it to only weakly affect scaling exponents – a result that further consolidates the here found link between connectivity eigenvalues and dynamics. This link holds qualitatively even in the strongly non-orthogonal regime (see IV C), especially for those observables of most interest to this work, such as the PC spectrum and dimensionality.

B. Fundamental, yet hidden structures

The eigenmode structures here discovered are of a new fundamental kind, which is different and largely complements traditional motifs. Their fundamental nature is exposed by our results in Section III and Section IV, respectively from a functional and structural perspective. Functionally, we have just revised how these structures largely complement motifs, controlling dynamical features inaccessible to the latter. But also structurally, these eigenmode structures are fundamentally different: their nature is *collective*, involving all connections concertedly, rather than *local*, involving connections between a few neurons. Indeed, we have shown in Section IV that, to leading order in the number of neurons, different shapes of the eigenvalue distribution and different degrees of eigenvectors’ non-orthogonality are in large part not reflected by local motifs.

Importantly, this last result exposes the existence of connectivity structures which, despite their high relevance for network dynamics, remain hidden to a traditional motif analysis. This poses solid theoretical grounds to look for these structures in connectivity data. These are revealed by an eigenmode analysis of the whole connectivity, which is accessible to experimental methods acquiring snapshots of a whole cortical microcircuit [42, 43]. A good surrogate of experimental data are digital reconstructions of cortical circuits [44], which are already being used to characterize local motif structures, like simplices [45].

C. Structure within randomness

The high heterogeneity of cortical microcircuits makes them appear, to a first approximation, as randomly connected and thus strikingly similar across cortical areas [9]. Analyses and models of their connectivity are thus faced with the paradox of identifying structure within this randomness. The results in Section IV provide a new insight into this paradox, showing that much structure can be encoded in the eigenmode statistics of an apparently random connectivity, while remaining hidden in the synaptic statistics.

Our random matrix theory enables direct control of these eigenmode structures, thus opening new possibilities for modeling cortical microcircuits. As shown in IV B, these structures represent new hidden features of connectivity, which can be fixed in addition to more traditional parameters, like the mean and variance of synaptic strengths, or the abundance of specific motifs. Note that fixing only these traditional parameters corresponds to implicitly making a particular choice for the eigenmode statistics, in particular selecting a uniform elliptical eigenvalue distribution. However, given the here discovered impact of the density of nearly critical eigenvalues on functionally relevant observables, it is sensible to explicitly fix this property of connectivity using our theory linking it to measurable power-law exponents. For example, in the case of V1, this density can be fixed to match the observed fine-tuning in the slope of the PC spectrum [3].

We have shown how these eigenmode structures have a profound impact on the dynamics, controlling previously inaccessible observables that are also found to be fine-tuned in brain networks. It would thus be interesting to further explore the effect of these structures on network dynamics, in particular their interplay with other features of neural networks, such as non-linear interactions, spiking neurons, or additional low rank structures, whether of an organized [18] or statistical nature like non-reciprocal second order motifs [11]. All of these features are readily added to the here studied system Eq. (1). In fact, we note that our method of modeling connectivity is general and can be implemented in many network models. In particular, it can also be adopted in

models implementing inhibitory and excitatory populations, as well as sparse connections. For example, the connectivity can be decomposed as $S \odot (J + M)$ [46], with S a Boolean random matrix indicating the presence of a synapse, implementing sparse connectivity, and M a low rank matrix encoding the inhibitory and excitatory mean synaptic strengths [11, 47]. In this case, the here studied random connectivity J models fluctuations around the mean synaptic strengths. This and similar extensions and generalizations will reveal the impact of the here found hidden structures in shaping the dynamics and function of other state-of-the-art neural network models.

ACKNOWLEDGMENTS

This work was partially supported by the Helmholtz Association, the Initiative and Networking Fund under project number SO-092 (Advanced Computing Architectures, ACA), and the German Federal Ministry for Education and Research (BMBF Grant 01IS19077A). Open access publication funded by the Deutsche Forschungsgemeinschaft (DFG, German Research Foundation) – 491111487.

Appendix A: Connectivity statistics

1. Details on the definition of the eigenmode statistics

Let us give the remaining details on the definition of the eigenmode statistics, presented in Section II. For simplicity, let us consider N even. Generalizing to N odd is straightforward. The realness of the elements of J imposes the condition that for any complex λ_α and V_α , there is an eigenmode index α^* such that $\lambda_{\alpha^*} = \lambda_\alpha^*$ and $V_{\alpha^*} = V_\alpha^*$. Note that since eigenmodes are randomly drawn in our ensemble, the probability that an eigenmode is real has null measure. Therefore we can assume all eigenmodes to be complex. By the constraint of real-valued J we only have $N/2$ eigenmodes that are independent. We assign these eigenmodes to the first $\alpha = 1, \dots, N/2$ of the eigenmode indices. The corresponding complex conjugate eigenmodes are assigned the index $\alpha^* = \alpha + N/2$. The first $N/2$ eigenvalues are drawn independently according to the desired distribution $p(\lambda)$. The remaining half is obtained by complex conjugation.

The matrix of eigenvectors V is a linear combination of O and G . The scheme by which these two matrices are defined is the same. Let us consider, for example, G . Only the first $\alpha = 1, \dots, N/2$ eigenvectors are independent, and each has a real and an imaginary component. So we need to draw $\frac{N}{2}2N = N^2$ random variables. We draw a real matrix γ whose entries $\gamma_{i\alpha} \sim \mathcal{N}(0, 1/N)$ are independent, normally distributed variables. The first

$\alpha = 1, \dots, N/2$ vectors $G_{\cdot,\alpha}$ are then defined as

$$G_{\cdot,\alpha} = \frac{1}{\sqrt{2}}\gamma_{\cdot,\alpha} + \frac{i}{\sqrt{2}}\gamma_{\cdot,\alpha+N/2}$$

In words, the first $\alpha = 1, \dots, N/2$ columns of γ constitute the real part of the vectors $G_{\cdot,\alpha}$, the remaining columns $\alpha + N/2$ constitute the imaginary part. The remaining vectors G_{\cdot,α^*} are obtained through complex conjugation.

The matrix O is defined in the same way, substituting $G \rightarrow O$ and $\gamma \rightarrow o$. The only difference is that o is a real orthonormal matrix, drawn from the Haar distribution (i.e. the uniform distribution over orthogonal matrices). One can easily check that O satisfies the complex orthonormality relation $OO^\dagger = \mathbb{I}$.

Let us note that here we considered eigenvalue distributions for which the mean $\langle \lambda \rangle = 0$. A non-vanishing mean is trivial, as it amounts to sending $J \rightarrow J + \langle \lambda \rangle \mathbb{I}$, which can be reabsorbed in the definition of the leak term $-x \rightarrow -(1 - \langle \lambda \rangle)x$ in Eq. (1).

We finally comment on J being diagonalizable, and on the left eigenvectors' matrix being the inverse of the right eigenvectors' matrix (cf. Eq. (3)). The subset of non-diagonalizable matrices has null measure. Therefore it has null probability, unless one assumes some very specific distribution that is singular on the subset, which is neither the case for our ensemble nor for the archetypal Gaussian ensemble. The same reasoning applies to the subset of matrices that have degenerate or null eigenvalues, or both. Therefore, left and right eigenvectors are inverse of each other if properly normalized. Note that here we are modeling the random part of a network's connectivity. In this case, we have shown that the aforementioned properties can be reasonably assumed. This is not necessarily the case, instead, if one is modeling specific structures that are added on top of the random connectivity, such as, for example, low rank perturbations [18].

2. Insights into the non-normality parameter ν

Here we give further intuition regarding the non-normality parameter ν and the specific definition Eq. (5) of the eigenvectors. This also allows us to get better insights into why the synaptic gain g diverges in the strongly non-normal regime $\nu \rightarrow 1$.

It is instructive to look at a naive approach in defining the eigenvector statistics. As we stated in Section II, we want to be agnostic regarding the direction taken by the random eigenvectors in neuronal space. The simplest - but too naive - way of implementing this would be to initialize $V = G$ as random Gaussians, rather than $V = O + \nu G$ as in Eq. (5). The problem is that eigenvectors defined in this way take on too random directions, having too strong overlaps. This causes the synaptic gain g to take on arbitrarily large values, when it should instead be of order unity to have physical meaning. One helpful way to visualize this is by looking at

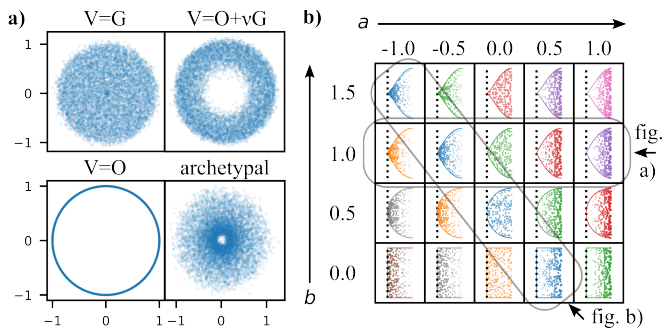


Figure A1. (a) Eigenvalues of the normalized eigenvector matrix V , for different choices of V . Parameters: $N = 10^2$. We show eigenvalues from 10^2 independent realizations of the eigenvectors. For the case $V = O + \nu G$, we use a value of $\nu = 0.8$. (b) Grid showing different distributions of nearly critical eigenvalues for varying a and b . Distributions with the same $d = a + b + 1$ share the same color (diagonals). We highlight the eigenvalue distributions used for the simulations in Fig. 3(a) (fixed b and varying a , i.e. varying d) and in Fig. 3(b) (fixed d and varying b).

the eigenvalues of V (Fig. A1(a)). For $V = G$, these are uniformly distributed in a circle, and can get arbitrarily close to zero (Fig. A1(a), top left). This means V^{-1} , which also appears in the definition of the connectivity J , Eq. (3), can have arbitrarily large eigenvalues, and is thus unbounded, causing also g to be unbounded as a consequence. On the other hand, notice that in the trivial case of a normal network, $V = O$, the eigenvalues are exactly constrained to the unit circle, and the problem does not occur (Fig. A1(a), bottom left). To have a well defined connectivity with $g = \mathcal{O}(1)$, we introduce non-orthogonality in the eigenvectors gradually, shifting away from the orthogonal case by increasing ν , through the choice $V = O + \nu G$. Notice that in this case the eigenvalues of V cannot get arbitrarily close to zero, but are constrained to be outside of an inner circle, which will shrink back to zero as $\nu \rightarrow 1$ (Fig. A1(a), top right). We observe the same mechanism occurring in the eigenvectors of the archetypal connectivity (Fig. A1(a), bottom right). Notice that in this case the inner circle has a very small radius, which in our approach would correspond to values of ν very close to 1 and a nonphysical synaptic gain $g = \mathcal{O}(\sqrt{N})$, diverging with the system size. In fact, as discussed in IV C, such strong degree of non-normality in the archetypal J is only achieved through a fine-tuned correlation between eigenvalues and eigenvectors, which ensures that all diverging contributions in Eq. (3) are tightly balanced.

3. Eigenvalue distributions used in simulations

Here we report the precise eigenvalue distributions used for the simulation of the dynamical quantities considered in Section III. Note that only the shape of the

distribution near criticality is important in determining the scaling properties of dynamical quantities. Such shape has been already reported in the main text and figures. The choice of the distribution for eigenvalues further away from criticality is arbitrary and irrelevant. We report it below for completeness.

For all quantities controlled by the exponent d , that is the density of nearly critical modes along the real axis, we used the following eigenvalue distribution

$$p(\mathbf{k}) = k_x^a \theta \left(S \left(1 - (1 - k_x)^2 \right)^b - |k_y| \right) \quad \forall k_x \leq 1, \quad (\text{A1})$$

with θ being the Heaviside function. Note that A1 obeys the asymptotic scaling 10 and 12 for nearly critical eigenvalues, with $d = a + b + 1$. The parameter S allows to stretch the distribution along the imaginary axis. It is fixed to 1 in all simulations, unless stated otherwise. In Fig. A1(b) we show the distribution for the first half of the eigenvalues ($0 < k_x < 1$), as a function of the parameters a and b . The remaining half of the eigenvalues, with $1 < k_x < 2$ and thus further away from criticality, are drawn in a symmetric manner: we send $k \rightarrow 2 - k$, draw the new variable according to Eq. (A1), and transform back to the original variable (see for example the distributions shown in Fig. 2). As stated above, the precise shape of the eigenvalue distribution in this second half of the complex plane is irrelevant. Thus, the specific choice of drawing eigenvalues in a symmetric manner is only taken for technical convenience, because then $\langle \lambda \rangle = 0$ and there is no need to rescale the leak term in Eq. (1) (see A1). In fact, even the precise shape of the distribution of the first half of the eigenvalues, Eq. (A1), is irrelevant: Only its limiting behavior for $k_x \rightarrow 0$ is important. The specific shape of the distribution has been chosen because for $a = 0$ and $b = 0.5$ it corresponds to a uniform elliptical distribution, as that of the archetypal J .

For all quantities controlled by the exponent \bar{d} , that is the density of nearly critical modes along the radial direction, we used the following eigenvalue distribution

$$p(\rho, \phi) = \rho^{\bar{d}-1} \theta \left(\arccos \left(\frac{\rho}{2} \right) - |\phi| \right) \quad \forall \rho \leq 1 \quad (\text{A2})$$

where $k \equiv \rho e^{i\phi}$. Note the expression in the Heaviside function constrains eigenvalues to lie within a circle. We fixed this shape for convenience, because for $\bar{d} = 2$ it reduces to the uniform distribution on the circle, as that of the archetypal J . Again, the exact shape of the distribution away from criticality is irrelevant, but we report it here for completeness. The remaining eigenvalues in the first half of the circle, i.e. with $1 < \rho < \sqrt{2}$, are drawn according to Eq. (A2), but are rejected and redrawn if they fall out of the semicircle, that is if $k_x > 1$. The remaining half of the eigenvalues are drawn symmetrically, as discussed in the paragraph above.

4. Strongly non-normal regime

Here we report details on the method presented in IVC, to numerically implement connectivities in the strongly non-normal regime that have a desired shape of the eigenvalue distribution. The method produces the distributions presented in A 3.

We start by initializing the archetypal Gaussian J , with $g = 1$ and $\tau = 0$. Its eigenvalues λ_α and associated right and left eigenvectors V_α and V_α^{-1} are derived numerically. The eigenvalues λ are uniformly distributed within a circle of unit radius. We start from this distribution and continuously shift the eigenvalues into some new position, so that they follow a new desired distribution. The continuous shift of the eigenvalues preserves to some extent the correlation structure between eigenvalues and eigenvectors, which in the strongly non-normal regime is necessary to have a synaptic gain $g = \mathcal{O}(1)$.

We first focus on producing the eigenvalue distribution Eq. (A1). This distribution is characterized by the parameters S , b and d (or equivalently a). The starting uniform circular distribution has parameters $S_0 = 1$, $b_0 = 0.5$ and $d_0 = 1.5$. Consider $k = 1 - \lambda$. To produce the eigenvalue distribution Eq. (A1) we shift the eigenvalues $k \rightarrow \bar{k}$ through the transformation

$$\bar{k}_x = k_x^{\frac{d_0}{d}} \quad (\text{A3})$$

$$\bar{k}_y = k_y \frac{B(\bar{k}_x; S, b)}{B(k_x; S_0, b_0)} \quad (\text{A4})$$

where we defined the distribution's boundary function

$$B(k_x; S, b) \equiv S \left(1 - (1 - k_x)^2\right)^b.$$

This transformation is applied to all eigenvalues with $k_x \leq 1$. The remaining half of the eigenvalues, with $1 < k_x < 2$, are transformed in the symmetric manner described in A 3. Intuitively, Eq. (A3) readjusts the eigenvalues closer or further to the critical point according to the new d . Eq. (A4) rescales the imaginary part so that it fits the new boundary of the distribution.

To obtain the distribution Eq. (A2) we use an analogous method, only that the transformation is performed on the polar coordinates of $k = \rho e^{i\phi}$. The target distribution is characterized by the parameter \bar{d} , and the original distribution has a parameter $\bar{d}_0 = 2$. We apply the transformation

$$\bar{\rho} = \rho^{\frac{\bar{d}_0}{\bar{d}}}$$

$$\bar{\phi} = \phi \frac{B(\bar{\rho})}{B(\rho)}$$

with boundary function

$$B(\rho) \equiv \arccos\left(\frac{\rho}{2}\right)$$

This transformation is applied to all eigenvalues with $\rho \leq 1$. As stated in A 3, the shape of the distribution

for eigenvalues further from criticality is arbitrary and irrelevant. We give it here for completeness. The remaining eigenvalues with $1 < \rho < \sqrt{2}$ which also are in the first semicircle $k_x \leq 1$ are left untouched. The remaining eigenvalues in the second semicircle are transformed in the symmetric manner described in A 3.

5. Derivation of the synaptic statistics

We develop a method to compute moments (or cumulants) of the matrix elements of J . The details are reported in Section I of the Supplemental Material [32]. Here we summarize the main ideas behind the method.

Looking at the definition Eq. (3), we can see that this involves being able to compute moments of the elements of the eigenvector matrix $V = O + \nu G$ and its inverse V^{-1} (commonly called the matrices of the right and left eigenvectors, respectively). For example, computing the second moment of J corresponds to

$$\langle J_{ij} J_{hk} \rangle = \sum_{\alpha\beta} \langle \lambda_\alpha \lambda_\beta \rangle_\lambda \left\langle V_{i\alpha} V_{\alpha j}^{-1} V_{h\beta} V_{\beta k}^{-1} \right\rangle_{O,G}$$

To proceed, we note that the inverse can be written as the infinite series

$$V^{-1} = \sum_{n=0}^{\infty} (-\nu)^n (O^\dagger G)^n O^\dagger,$$

where we used that O is unitary. Computing a certain moment of V and V^{-1} thus corresponds to computing an infinite number of moments of O and G . Being Gaussian, the moments of G can be computed using Wick calculus [48], that is using the known result that moments of G factorize into the expectation of pairs of G , summing over all possible ways of pairing the G s. Similarly, moments of O can be computed using Weingarten calculus [49–51], the analogous of Wick calculus for orthogonal matrices. Weingarten calculus is more complicated, but in the limit of large N it reduces to leading order to Wick calculus [49].

There is still an infinite number of moments to compute and, at each order of ν , a large number of terms arising from the combinatorics involved in Wick calculus. At each order of ν , however, only a few terms are of leading order in N . Using a Feynman-diagram representation [48], we are able to keep track of these leading order terms, which can be identified based on the topology of the associated diagrams. Once the terms of leading order in N are computed for any given order of ν , we are able to resum all orders of ν exactly. Note that therefore our results are exact in ν and perturbative in N , which is naturally large.

With this method, we compute the second moments of J , Eq. (6) and Eq. (7). In IE of the Supplemental Material [32], we also compute the third cumulants of J . We do not compute explicitly higher order moments of J . Computing these would involve considering subleading

order deviations of Weingarten calculus from Wick calculus. However, we are able to use the properties of the full Weingarten calculus to prove the results presented in IV B, i.e. identifying which higher order moments do not vanish, and proving that these non-vanishing moments are still of subleading order in N .

Appendix B: Derivation of dynamical quantities

Here we give details on the derivation of the dynamical quantities considered in Section III.

1. Autocorrelation and autoresponse

Let us start by considering the system's linear response matrix $R(t)$, which is the Green function of Eq. (1). In frequency domain this is defined as the solution to

$$(i\omega\mathbb{I} + \mathbb{I} - J)R(\omega) = \mathbb{I}, \quad (\text{B1})$$

which is

$$R(\omega) = (i\omega\mathbb{I} + \mathbb{I} - J)^{-1}. \quad (\text{B2})$$

Using the eigenmode decomposition of J , Eq. (3), we can rewrite Eq. (B2) as

$$R_{ij}(\omega) = \sum_{\alpha} \frac{1}{i\omega + k_{\alpha}} V_{i\alpha} V_{\alpha j}^{-1} \quad (\text{B3})$$

which in time domain reads

$$R_{ij}(t) = \sum_{\alpha} \exp(-k_{\alpha}t) V_{i\alpha} V_{\alpha j}^{-1} \quad (\text{B4})$$

The expression for the population averaged autoresponse Eq. (8), considered in III A, directly follows from computing $r(t) = \frac{1}{N} \sum_i R_{ii}(t)$, noticing that $\sum_i V_{i\alpha} V_{\alpha i}^{-1} = \delta_{\alpha,\alpha} = 1$. The latter identity makes $r(t)$ independent of the eigenvectors.

Let us now consider the time-lagged covariance matrix $C_{ij}(t) \equiv \langle x_i(t) x_j(0) \rangle_{\xi}$. This can be derived by plugging into its definition the formal solution $x_i(t) = \int_{t'} \sum_j R_{ij}(t-t') \xi_j(t')$ and averaging over the noise. In frequency domain, the result is

$$C(\omega) = (i\omega\mathbb{I} + \mathbb{I} - J)^{-1} (i\omega\mathbb{I} + \mathbb{I} - J)^{-\dagger} \quad (\text{B5})$$

Using the eigenmode decomposition of J , Eq. (3), we can rewrite Eq. (B5) as

$$C_{ij}(\omega) = \sum_{\alpha\beta} F_{\alpha\beta}(\omega) V_{i\alpha} \left(\sum_h V_{\alpha h}^{-1} V_{\beta h}^{-1} \right) V_{j\beta},$$

$$F_{\alpha\beta}(\omega) \equiv \frac{1}{(\omega - ik_{\alpha})(\omega + ik_{\beta})} \quad (\text{B6})$$

which in time domain reads

$$C_{ij}(t) = \sum_{\alpha\beta} F_{\alpha\beta}(t) V_{i\alpha} \left(\sum_h V_{\alpha h}^{-1} V_{\beta h}^{-1} \right) V_{j\beta},$$

$$F_{\alpha\beta}(t) \equiv \frac{\theta(t) \exp(-k_{\alpha}t) + \theta(-t) \exp(k_{\beta}t)}{k_{\alpha} + k_{\beta}}. \quad (\text{B7})$$

The population averaged autocorrelation considered in III A is given by $A(t) = \frac{1}{N} \sum_i C_{ii}(t)$, which reads

$$A(t) = \frac{1}{N} \sum_{\alpha\beta} F_{\alpha\beta}(t) L_{\alpha\beta}, \quad (\text{B8})$$

where we defined the so-called overlap matrix

$$L_{\alpha\beta} = \sum_i V_{i\alpha} V_{i\beta} \sum_h V_{\alpha h}^{-1} V_{\beta h}^{-1} \quad (\text{B9})$$

which is a measure of how much different modes overlap in neuronal space. It is diagonal in the case $\nu = 0$ of orthonormal $V = O$. For large number of neurons N , A is self-averaging, meaning $A \sim \langle A \rangle_{O,G}$ apart from fluctuations of subleading order in N . In the expression for A , Eq. (B8), we can therefore substitute L with $\langle L \rangle_{O,G}$. The latter we can compute using the same methods summarized in A 5 (see II A of the Supplemental Material [32] for the derivation). The result is, to leading order in N ,

$$\langle L_{\alpha\beta} \rangle = \frac{1 + \nu^2}{1 - \nu^2} \delta_{\beta,\alpha^*} - \frac{2}{N} \frac{\nu^2}{1 - \nu^2}. \quad (\text{B10})$$

As commented in III A, the first term is the only one present in the limit of orthonormal eigenvectors $\nu \rightarrow 0$, while the second term reflects a non-vanishing overlap between eigenvectors for any other $\nu \neq 0$. Eq. (9) in III A is obtained by plugging Eq. (B10) into Eq. (B8) and taking the limit of the sum over eigenvalues to an integral over their probability density, with integration measure $\mathcal{D}k \equiv p(k) dk$.

2. Dimensionality

Let us recall the definition of the participation ratio for a generic covariance matrix C

$$D \equiv \frac{(\text{Tr}[C])^2}{\text{Tr}[C^2]}. \quad (\text{B11})$$

For the equal-time covariance, C corresponds to $C(t=0)$ given by Eq. (B7), while for the long time-window covariance C corresponds to $C(\omega=0)$ given by Eq. (B6).

Equal-time covariance As noted in III B, for the equal-time covariance, the numerator $(\text{Tr}[C])^2$ corresponds to $A(t=0)^2$ given in Eq. (9), whose diverging behavior near criticality is discussed in Eq. (11). Using Eq. (B7) the expression for the denominator reads

$$\text{Tr}[C^2] = \frac{1}{N^2} \sum_{\alpha\beta\gamma\delta} F_{\alpha\beta}(t=0) F_{\gamma\delta}(t=0) L_{\alpha\beta\gamma\delta}^{(2)}, \quad (\text{B12})$$

where we defined the overlap tensor

$$L_{\alpha\beta\gamma\delta}^{(2)} = \sum_i V_{i\alpha} V_{i\gamma} \sum_j V_{j\beta} V_{j\delta} \sum_h V_{\alpha h}^{-1} V_{\beta h}^{-1} \sum_k V_{\gamma k}^{-1} V_{\delta k}^{-1}. \quad (\text{B13})$$

Also $\text{Tr}[C^2]$ is self-averaging, so we can substitute $L^{(2)}$ with $\langle L^{(2)} \rangle_{O,G}$ and compute it with the same methods used for $\langle L \rangle_{O,G}$. The full result and its derivation are lengthy and are reported in IIB of the Supplemental Material [32]. Here we only report the term that dominates in the diverging behavior of $\text{Tr}[C^2]$ near criticality

$$\langle L_{\alpha\beta\gamma\delta}^{(2)} \rangle_{O,G} \sim \left(\frac{1 + \nu^2}{1 - \nu^2} \right)^2 \delta_{\beta,\alpha^*} \delta_{\gamma,\alpha^*} \delta_{\delta,\alpha}$$

which plugged into Eq. (B12) gives Eq. (16) in IIIB.

Long time-window covariance The reasoning for the long time-window covariance is completely analogous. By comparing Eq. (B7) with Eq. (B6) we notice that one simply needs to replace $F_{\alpha\beta}(t=0) \rightarrow F_{\alpha\beta}(\omega=0)$. This leads to the results given in IIIB. Notice that, while $F_{\alpha\alpha^*}(t=0) = \frac{1}{\text{Re}k_\alpha}$, instead $F_{\alpha\alpha^*}(\omega=0) = \frac{1}{|k_\alpha|^2}$, so the relevant direction along which to approach criticality is the radial one, instead of the real axis.

3. Principal components spectrum

From Eq. (B7) and Eq. (B6) we immediately see that for $\nu=0$ the eigenvalues c_α of the equal time or long time-window covariance are, respectively, $F_{\alpha\alpha^*}(t=0) = \frac{1}{\text{Re}k_\alpha}$ and $F_{\alpha\alpha^*}(\omega=0) = \frac{1}{|k_\alpha|^2}$. Indeed, for $\nu=0$ the eigenvectors are orthonormal and so the term $\sum_h V_{\alpha h}^{-1} V_{\beta h}^{-1} = \delta_{\beta,\alpha^*}$. From this observation follow the results discussed in IIIC.

Appendix C: Additional figures

Here we provide some supplementary figures. Further supplementary figures are provided in the Supplemental Material [32].

Fig. C1 shows the qualitative irrelevance of details in the eigenmode statistics beyond the density of nearly critical eigenmodes in controlling the dynamical quantities studied in Section III. In particular, Fig. C1(a) shows the autoresponse and autocorrelation functions for different connectivities, which share the same density of nearly critical eigenvalues, but differ in other properties: we consider different relative spreads of the eigenvalues along the imaginary and real axis, controlling the level of symmetry in the connectivity, along with different levels of non-normality. Even if these parameters vary, the power-law decay of both functions is only controlled by d and remains the same. Analogously, Fig. C1(b) shows that the slope in the PC spectrum does not change for different relative spreads or different shapes of the boundary of the eigenvalue distribution. Figures Fig. C1(c-d)

show dimensionality as all of the aforementioned parameters are varied. Again, while we have quantitative differences, the qualitative behavior of dimensionality is not altered. The transition from high to low dimensionality still occurs at $d=2$, and a clear minimum is present at $d \sim 1$.

Fig. C2 shows a numerical validation of our analytical predictions for the motifs statistics. A connectivity with an asymmetric eigenvalue distribution is chosen, so that third order motifs do not vanish. The numerics for the strongly non-normal regime are also reported and compared with the predictions for our ensemble. Notice that simulations agree well with theory. Also in the case of the strongly non-normal connectivity, we have a qualitative agreement for the non-vanishing motifs, and even a quantitative agreement for the motifs that are expected to vanish exactly (see the red markers partially hidden below the blue markers). Note that the values of the third and fourth order cumulants are shown rescaled by a factor \sqrt{N} and N , respectively. The fact that they are of order unity in the plot, therefore, validates our prediction that these higher order motifs are subleading in the number of neurons.

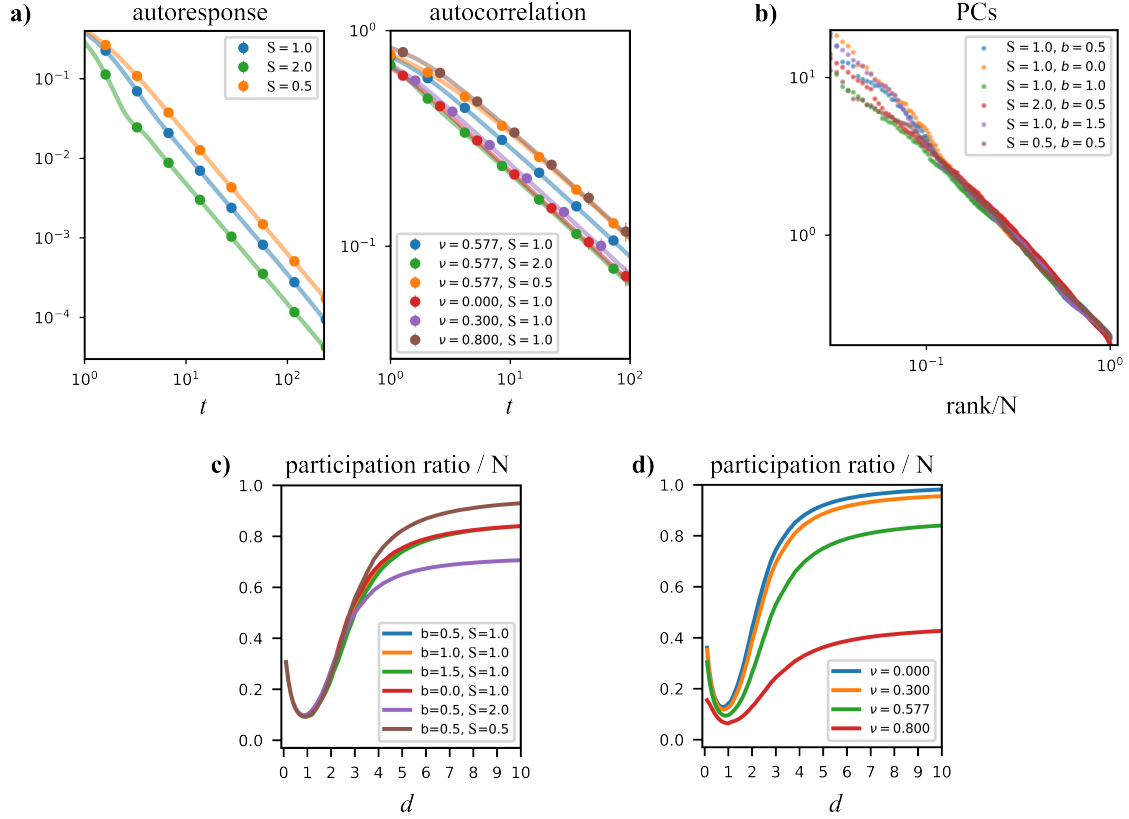


Figure C1. Irrelevance of details in the shape of the eigenvalue distribution and the degree of non-normality. (a) Autoresponse and autocorrelation, for $d = 1.5$. Shown for varying stretching factor S of the eigenvalue distribution along the imaginary axis (cfr. Eq. (A1)) and for varying degree of non-normality ν (autocorrelation only). Markers: simulation; full curves: theory. Other parameters: $b = 1.0, N = 10^2$. (b) Principal component spectrum of the equal-time covariance, for $d = 1.0$. Shown for varying S and varying b , controlling the boundary of the eigenvalue distribution (cfr. Eq. (12)). Other parameters: $\nu = 1/\sqrt{3}, N = 4 \cdot 10^2, \delta = 0.01$. (c) Dimensionality of the equal-time covariance, for $\delta = 0.01$. Shown for varying S and b . Full curves: theory. Other parameters: $\nu = 1/\sqrt{3}$. (d) Dimensionality of the equal-time covariance, for $\delta = 0.01$. Shown for varying ν . Full curves: theory. Other parameters: $S = 1, b = 0.5$.

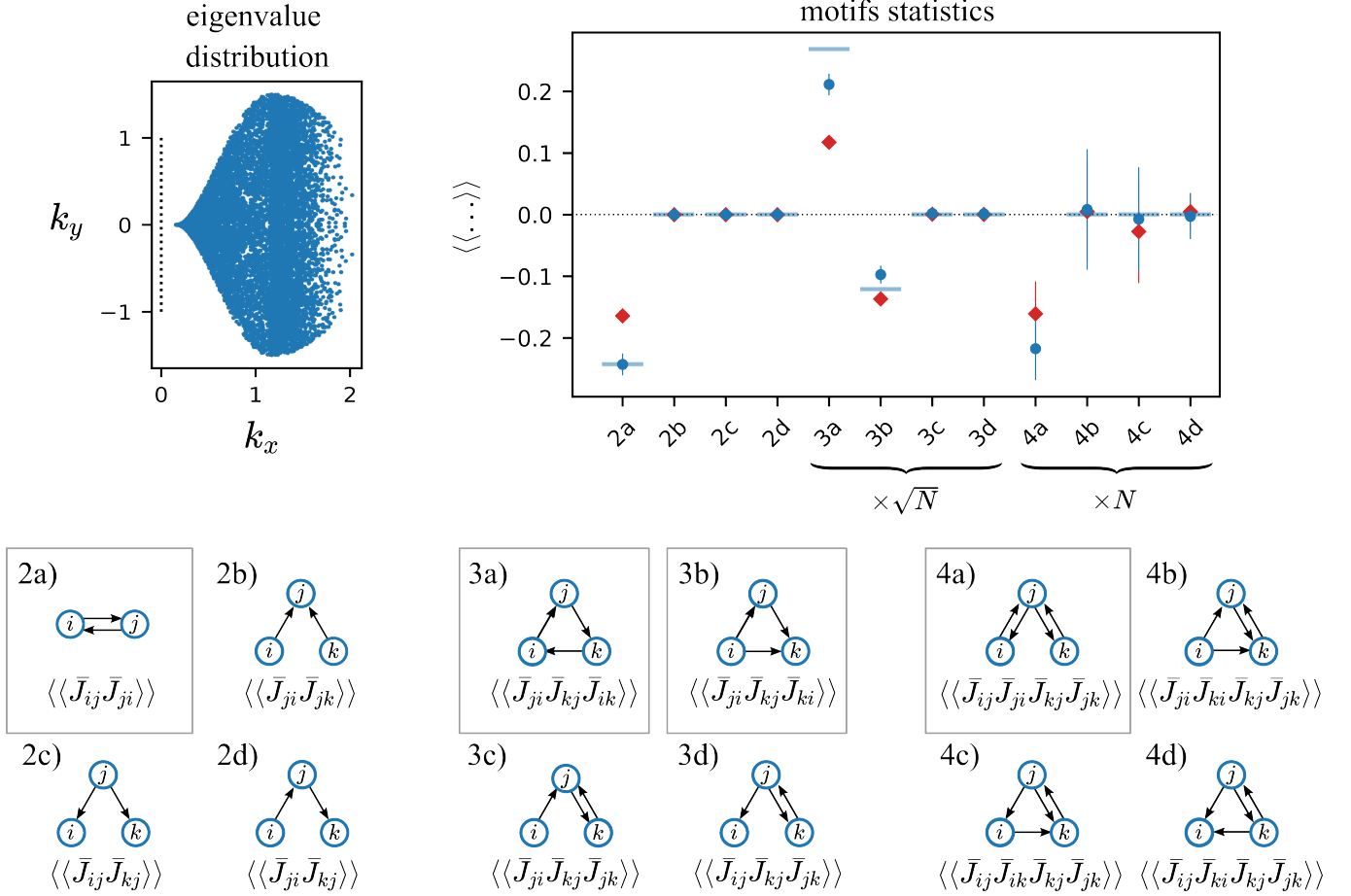


Figure C2. Motifs statistics. Bottom: catalog of all motifs up to fourth order involving up to three different neurons, alongside with the associated cumulant of the normalized synaptic strengths matrix \bar{J} (cf. IV B). Top: empirical measurement of these cumulants (i.e. averaging over synapses within a single connectivity realization), for a connectivity with eigenvalue distribution shown on the left. Blue dots: case of a connectivity in our ensemble, for $\nu = 0.577$; red dots: case of a connectivity in the strongly non-normal ensemble. Note that third and fourth order cumulants are plotted, rescaled by a factor \sqrt{N} and N , respectively. Blue dash: theoretical prediction for the original ensemble. All motifs that are not highlighted with boxes in the bottom catalog are predicted by our theory to vanish exactly. For the non-vanishing motifs up to third order, the analytical prediction is given by Eq. (7) for the second order motifs and equations (S25-S26) in the Supplemental Material [32] for the third order motifs.

- [1] S. N. Dorogovtsev, A. V. Goltsev, and J. F. F. Mendes, Critical phenomena in complex networks, *Rev. Mod. Phys.* **80**, 1275 (2008).
- [2] E. R. Kandel, J. H. Schwartz, T. M. Jessell, S. A. Siegelbaum, A. Hudspeth, and S. Mack, *Principles of Neural Science*, 5th ed. (McGraw-Hill, New York, 2013).
- [3] C. Stringer, M. Pachitariu, N. Steinmetz, M. Carandini, and K. D. Harris, High-dimensional geometry of population responses in visual cortex, *Nature* **571**, 361 (2019).
- [4] P. T. Sadtler, K. M. Quick, M. D. Golub, S. M. Chase, S. I. Ryu, E. C. Tyler-Kabara, B. M. Yu, and A. P. Batista, Neural constraints on learning, *Nature* **512**, 423 (2014), number: 7515 Publisher: Nature Publishing Group.
- [5] J. A. Gallego, M. G. Perich, S. N. Naufel, C. Ethier, S. A. Solla, and L. E. Miller, Cortical population activity within a preserved neural manifold underlies multiple motor behaviors, *Nat. Commun.* **9**, 1 (2018).
- [6] J. D. Smedo, A. Zandvakili, C. K. Machens, M. Y. Byron, and A. Kohn, Cortical areas interact through a communication subspace, *Neuron* **102**, 249 (2019).
- [7] M. Rigotti, O. Barak, M. R. Warden, X.-J. Wang, N. D. Daw, E. K. Miller, and S. Fusi, The importance of mixed selectivity in complex cognitive tasks, *Nature* **497**, 585 (2013).
- [8] B. Sorscher, S. Ganguli, and H. Sompolinsky, Neural representational geometry underlies few-shot concept learning, *Proceedings of the National Academy of Sciences* **119**, e2200800119 (2022).
- [9] V. Braitenberg and A. Schüz, *Anatomy of the Cortex: Statistics and Geometry* (Springer-Verlag, Berlin, Heidelberg, New York, 1991).
- [10] Y. Hu, J. Trousdale, K. Josić, and E. Shea-Brown, Motif statistics and spike correlations in neuronal networks, *J. Stat. Mech. Theory Exp.* **2013**, P03012 (2013).
- [11] Y. Hu and H. Sompolinsky, The spectrum of covariance matrices of randomly connected recurrent neuronal networks with linear dynamics, *PLOS Computational Biology* **18**, 1 (2022).
- [12] D. Dahmen, S. Recanatesi, X. Jia, G. K. Ocker, L. Campaignola, T. Jarsky, S. Seeman, M. Helias, and E. Shea-Brown, Strong and localized recurrence controls dimensionality of neural activity across brain areas, *BioRxiv* (2022).
- [13] S. Song, P. Sjöström, M. Reigl, S. Nelson, and D. Chklovskii, Highly nonrandom features of synaptic connectivity in local cortical circuits, *PLOS Biol.* **3**, e68 (2005).
- [14] J. M. Beggs and D. Plenz, Neuronal avalanches in neocortical circuits, *J. Neurosci.* **23**, 11167 (2003).
- [15] L. Meshulam, J. L. Gauthier, C. D. Brody, D. W. Tank, and W. Bialek, Coarse graining, fixed points, and scaling in a large population of neurons, *Phys. Rev. Lett.* **123**, 178103 (2019).
- [16] A. J. Fontenele, N. A. P. de Vasconcelos, T. Feliciano, L. A. A. Aguiar, C. Soares-Cunha, B. Coimbra, L. Dalla Porta, S. Ribeiro, A. J. Rodrigues, N. Sousa, P. V. Carelli, and M. Copelli, Criticality between cortical states, *Phys. Rev. Lett.* **122**, 208101 (2019).
- [17] G. Hennequin, T. Vogels, and W. Gerstner, Optimal control of transient dynamics in balanced networks supports generation of complex movements, *Neuron* **82**, 1394 (2014).
- [18] F. Mastrogiuseppe and S. Ostojic, Linking connectivity, dynamics, and computations in low-rank recurrent neural networks, *Neuron* **99**, 609 (2018).
- [19] B. Lindner, B. Doiron, and A. Longtin, Theory of oscillatory firing induced by spatially correlated noise and delayed inhibitory feedback, *Phys. Rev. E* **72**, 061919 (2005).
- [20] V. Pernice, B. Staude, S. Cardanobile, and S. Rotter, How structure determines correlations in neuronal networks, *PLOS Comput. Biol.* **7**, e1002059 (2011).
- [21] V. Pernice, B. Staude, S. Cardanobile, and S. Rotter, Recurrent interactions in spiking networks with arbitrary topology, *Phys. Rev. E* **85**, 031916 (2012).
- [22] D. Grytskyy, T. Tetzlaff, M. Diesmann, and M. Helias, A unified view on weakly correlated recurrent networks, *Front. Comput. Neurosci.* **7**, 131 (2013).
- [23] J. Trousdale, Y. Hu, E. Shea-Brown, and K. Josic, Impact of network structure and cellular response on spike time correlations, *PLOS Comput. Biol.* **8**, e1002408 (2012).
- [24] D. Dahmen, S. Grün, M. Diesmann, and M. Helias, Second type of criticality in the brain uncovers rich multiple-neuron dynamics, *Proc. Natl. Acad. Sci. USA* **116**, 13051 (2019).
- [25] H. Sompolinsky, A. Crisanti, and H. J. Sommers, Chaos in random neural networks, *Phys. Rev. Lett.* **61**, 259 (1988).
- [26] H. Sommers, A. Crisanti, H. Sompolinsky, and Y. Stein, Spectrum of large random asymmetric matrices, *Phys. Rev. Lett.* **60**, 1895 (1988).
- [27] G. Hennequin, T. Vogels, and W. Gerstner, Non-normal amplification in random balanced neuronal networks, *Phys. Rev. E* **86**, 011909 (2012).
- [28] D. R. Chialvo, Emergent complex neural dynamics, *Nat. Phys.* **6**, 744 (2010), number: 10 Publisher: Nature Publishing Group.
- [29] C. G. Langton, Computation at the edge of chaos: phase transitions and emergent computation, *Physica D* **42**, 12 (1990).
- [30] N. Bertschinger and T. Natschläger, Real-time computation at the edge of chaos in recurrent neural networks, *Neural Comput.* **16**, 1413 (2004).
- [31] T. Toyozumi and L. F. Abbott, Beyond the edge of chaos: Amplification and temporal integration by recurrent networks in the chaotic regime, *Phys. Rev. E* **84**, 051908 (2011).
- [32] See Supplemental Material for supplementary figures and further details on the analytical derivations.
- [33] K. G. Wilson, The renormalization group: Critical phenomena and the kondo problem, *Rev. Mod. Phys.* **47**, 773 (1975).
- [34] P. C. Hohenberg and B. I. Halperin, Theory of dynamic critical phenomena, *Rev. Mod. Phys.* **49**, 435 (1977).
- [35] U. C. Taeuber, *Critical dynamics: a field theory approach to equilibrium and non-equilibrium scaling behavior* (Cambridge University Press, 2014).
- [36] C. Haldeman and J. M. Beggs, Critical branching captures activity in living neural networks and maximizes the number of metastable states, *Phys. Rev. Lett.* **94**,

- 058101 (2005).
- [37] S. Chung, D. D. Lee, and H. Sompolinsky, Classification and geometry of general perceptual manifolds, *Phys. Rev. X* **8** (2018), 10.1103/physrevx.8.031003.
- [38] G. B. Morales and M. A. Muñoz, Optimal input representation in neural systems at the edge of chaos, *Biology* **10** (2021), 10.3390/biology10080702.
- [39] S. Bradde, F. Caccioli, L. Dall’Asta, and G. Bianconi, Critical fluctuations in spatial complex networks, *Phys. Rev. Lett.* **104**, 218701 (2010).
- [40] A. i. e. i. f. Tuncer and A. m. c. Erzan, Spectral renormalization group for the gaussian model and ψ^4 theory on nonspatial networks, *Phys. Rev. E* **92**, 022106 (2015).
- [41] B. A. Brinkman, Non-perturbative renormalization group analysis of nonlinear spiking networks, arXiv preprint arXiv:2301.09600 (2023).
- [42] M. Berning, K. M. Boergens, and M. Helmstaedter, SegEM: Efficient image analysis for high-resolution connectomics, *Neuron* **87**, 1193 (2015).
- [43] W. Yin, D. Brittain, J. Borseth, M. E. Scott, D. Williams, J. Perkins, C. S. Own, M. Murfitt, R. M. Torres, D. Kapner, *et al.*, A petascale automated imaging pipeline for mapping neuronal circuits with high-throughput transmission electron microscopy, *Nature communications* **11**, 4949 (2020).
- [44] H. Markram, E. Muller, S. Ramaswamy, M. W. Reimann, M. Abdellah, C. A. Sanchez, A. Ailamaki, L. Alonso-Nanclares, N. Antille, S. Arsever, G. A. A. Kahou, T. K. Berger, A. Bilgili, N. Buncic, A. Chalimourda, G. Chindemi, J.-D. Courcol, F. Delalondre, V. Delattre, S. Druckmann, R. Dumusc, J. Dynes, S. Eilemann, E. Gal, M. E. Gevaert, J.-P. Ghobril, A. Gidon, J. W. Graham, A. Gupta, V. Haenel, E. Hay, T. Hejnisch, J. B. Hernando, M. Hines, L. Kanari, D. Keller, J. Kenyon, G. Khazen, Y. Kim, J. G. King, Z. Kisvarday, P. Kumbhar, S. Lasserre, J.-V. L. Bé, B. R. Magalhães, A. Merchán-Pérez, J. Meystre, B. R. Morrice, J. Muller, A. Muñoz-Céspedes, S. Muralidhar, K. Muthurasa, D. Nachbaur, T. H. Newton, M. Nolte, A. Ovcharenko, J. Palacios, L. Pastor, R. Perin, R. Ranjan, I. Riachi, J.-R. Rodríguez, J. L. Riquelme, C. Rössert, K. Sfyarakis, Y. Shi, J. C. Shillcock, G. Silberberg, R. Silva, F. Tauheed, M. Telefont, M. Toledo-Rodriguez, T. Tränkler, W. V. Geit, J. V. Díaz, R. Walker, Y. Wang, S. M. Zaninetta, J. DeFelipe, S. L. Hill, I. Segev, and F. Schürmann, Reconstruction and simulation of neocortical microcircuitry, *Cell* **163**, 456 (2015).
- [45] A. Ecker, D. E. Santander, S. Bolaños-Puchet, J. B. Isbister, and M. W. Reimann, Cortical cell assemblies and their underlying connectivity: an in silico study, *bioRxiv*, 2023 (2023).
- [46] I. D. Harris, H. Meffin, A. N. Burkitt, and A. D. Peterson, Eigenvalue spectral properties of sparse random matrices obeying dale’s law, arXiv preprint arXiv:2212.01549 (2022).
- [47] J. Kadmon and H. Sompolinsky, Transition to chaos in random neuronal networks, *ArXiv*, 1508.06486 (2015).
- [48] M. Helias and D. Dahmen, *Statistical Field Theory for Neural Networks* (Springer International Publishing, 2020) p. 203.
- [49] D. Weingarten, Asymptotic behavior of group integrals in the limit of infinite rank, *Journal of Mathematical Physics* **19**, 999 (1978), publisher: American Institute of Physics.
- [50] B. Collins and P. Śniady, Integration with Respect to the Haar Measure on Unitary, Orthogonal and Symplectic Group, *Communications in Mathematical Physics* **264**, 773 (2006).
- [51] S. Matsumoto, Jucys-murphy elements, orthogonal matrix integrals, and jack measures, *The Ramanujan Journal* **26**, 69 (2011).